communications biology

Article

https://doi.org/10.1038/s42003-025-07566-2

Maternal immune activation followed by peripubertal stress combinedly produce reactive microglia and confine cerebellar cognition

Check for updates

Momoka Hikosaka[1], Md Sorwer Alam Parvez[1,2,12], Yuki Yamawaki[1,12], Souichi Oe[3], Yuan Liang[1,4], Yayoi Wada[1], Yukie Hirahara[3], Taro Koike[3], Hirohiko Imai[5,6], Naoya Oishi[7,8], Sina M. Schalbetter[9], Asuka Kumagai[10], Mari Yoshida[11], Takeshi Sakurai[1], Masaaki Kitada[3], Urs Meyer[9], Shuh Narumiya[1] & Gen Ohtsuki[1] ✉

The functional alteration of microglia arises in brains exposed to external stress during early development. Pathophysiological findings of neurodevelopmental disorders such as schizophrenia and autism spectrum disorder suggest cerebellar functional deficits. However, the link between stress-induced microglia reactivity and cerebellar dysfunction is missing. Here, we investigate the developmental immune environment in translational mouse models that combine two risk factors: maternal infection and repeated social defeat stress (2HIT). We find the synergy of inflammatory stress insults, leading to microglial increase specifically in the cerebellum of both sexes. Microglial turnover correlates with the Purkinje neuron loss in 2HIT mice. Highly multiplexed imaging-mass-cytometry identifies a cell transition to TREM2(+) stress-associated microglia in the cerebellum. Single-cell-proteomic clustering reveals IL-6- and TGFβ-signaling association with microglial cell transitions. Reduced excitability of remaining Purkinje cells, cerebellum-involved brain-wide functional dysconnectivity, and behavioral abnormalities indicate cerebellar cognitive dysfunctions in 2HIT animals, which are ameliorated by both systemic and cerebellum-specific microglia replacement.

Mental disorders cause significant disturbances in thinking, emotion, and behavior. Cumulative immune activation from both infectious and social defeating stress increases the risk for schizophrenia[1–5]. A disease-biased heterogeneity of microglia in the brain is considered one of the key mechanisms of mental disorders, as well as neurodegenerative diseases[6–8]. Although changes in microglial morphology and gene expression have been argued in the observations of postmortem brains with psychiatric disorders and translational animals, their reactivity, and neural and cognitive dysfunctions remain unclear.

In an animal model, offspring delivered from dams which had been exposed to maternal immune activation (MIA) during pregnancy exhibited severe social behavior anomalies. This phenotype resembles symptoms seen in human patients with developmental disorders who experienced extrinsic stressors, such as viral and microorganism infections in the sensitive period[9–12]. Another stress model for a mood disorder, repeated social defeat stress (RSDS), induces depressive-like behavior in mice[13,14]. These two models are commonly used for studying psychiatric disorder phenotypes in animals, mostly alone. There is ample evidence suggesting that a single

[1]Department of Drug Discovery Medicine, Kyoto University, Graduate School of Medicine, Kyoto, Japan. [2]Graduate Biomedical Sciences, University of Alabama at Birmingham, Birmingham, AL, USA. [3]Department of Anatomy, Kansai Medical University, Hirakata-shi, Osaka, Japan. [4]Institute of Basic Theory in Chinese Medicine, China Academy of Chinese Medical Sciences, Beijing, China. [5]Department of Systems Science, Kyoto University Graduate School of Informatics, Yoshida-Honmachi, Kyoto, Japan. [6]Innovation Research Center for Quantum Medicine, Gifu University School of Medicine, Gifu, Japan. [7]Department of Psychiatry, Kyoto University Graduate School of Medicine, Kyoto, Japan. [8]Human Brain Research Center, Kyoto University Graduate School of Medicine, Kyoto, Japan. [9]Institute of Veterinary Pharmacology and Toxicology, University of Zurich, Zurich, Switzerland. [10]Standard BioTools Inc., Chuo-ku, Tokyo, Japan. [11]Department of Neuropathology, Institute for Medical Science of Aging, Aichi Medical University, Nagakute, Aichi, Japan. [12]These authors contributed equally: Md Sorwer Alam Parvez, Yuki Yamawaki. ✉e-mail: ohtsuki.gen.7w@kyoto-u.ac.jp

factor does not fully account for the development of psychiatric disorders; instead, their onset results from the combination of multiple factors[1,2,15–17]. An epidemiological study suggests an increased risk of schizophrenia following exposure to environmental stress combined with prenatal infection and trauma after growth during the period of peripuberty (from age 8 to 14 years)[2]. Notably, prenatal infection alone does not lead to schizophrenia in men, and the interaction between prenatal infection and traumatizing experience was specific for boys[2]. Therefore, we hypothesized that combined stress plays a crucial role in the development of cognitive-affective disorders.

Microglia are the primary immune cells involved in brain dysfunctions[7,17–23]. Microglia are essential for host defense and scavenging the damage-, pathogen-, and neurodegeneration-associated molecular patterns in innate immunity[24,25]. Recent transcriptomic and morphological identifications conceptualized the heterogeneity of microglia across brain regions, sex differences, developmental stages, and the health-disease axis[25–28]. Sex differences are particularly important for neural circuit refinement during development[29]. Both rat and mouse models[30,31], as well as human patients with schizophrenia[32], suggest a blunting of microglial morphology and an increase in microglial density in response to inflammatory and pathological stresses. Prenatal immune stress epigenetically alters transcriptomes requisite for microglial immune reactivity[31], while we must note the differences between species. Additionally, many studies overlooked cerebellar microglia.

The cerebellum is increasingly recognized as a region potentially linked to mental disorders, including schizophrenia- and autism-spectrum disorders[33–37]. Traditionally, the cerebellum is indispensable for motor coordination, motor learning, and spatiotemporal prediction. Multi-dimensional phase compensations, enabled by ubiquitous plasticity within the circuit, may underlie its higher-order functions[38–40]. Recent studies have also associated cerebellar dysfunction with cognitive deficits and mental disorders[8,40]. In the early development of the cerebellum, microglia contribute to the removal of dead neurons and excess synapses[41–43], perhaps, in a sex-dependent manner[29]. However, sex-specific differences in stress responses are not well understood. Localized acute inflammatory stimulation of the cerebellum can modulate Purkinje cell activity, leading to behavioral disturbances in animals[44]. Chronic effects of inflammatory stress from the combined impact of such stress, however, remain unexplored. Here, we attempt to disentangle the synergistic effect of environmental stress in double-hit models (*i.e.*, the 2HIT model). The current studies suggest that in the 2HIT model, MIA blunts microglia[31], and the subsequent stress reactivates it[1]. We investigate if the cerebellum is vulnerable to accumulating two different stressors and if suppressing brain abnormality-related immunity in this specific region can alleviate the disturbances.

Results

Microglia proliferation and altered morphology in the cerebellum

To investigate a synergistic effect of extrinsic stresses, we produced mouse models exposed to either MIA, RSDS, or both (Fig. 1a and Supplementary Fig. 1a-e). We administered polyinosinic:polycytidylic acid (poly(I:C)) (10 mg/kg) to pregnant dams at embryonic day (E)12.5 to induce the MIA mouse model. Male offspring received defeat stress for ten consecutive days from an aggressive stressor at early puberty (RSDS, 4-week-old) (Fig. 1a) or at maturity (9-week-old; Supplementary Figs. 1a and 23a,b). The proportions of susceptible male mice were 63.2% in RSDS alone ($n = 19$) and 96.8% in 2HIT-conditioning ($n = 63$) when exposed to RSDS at 4 weeks, suggesting a synergistic effect of the two stresses. In contrast, when exposed to RSDS at 9 weeks of age, the proportions of susceptible mice were 50% for RSDS alone ($n = 22$) and 73.3% for 2HIT-conditioned ($n = 15$) groups, suggesting high vulnerability to RSDS at 4 weeks in the peripubertal period (Fig. 1b and Supplementary Fig. 1f–o). Unless otherwise stated, we adopted RSDS conditioning at 4 weeks old in subsequent studies. For female mice, susceptibility rates were 37.9% with RSDS alone ($n = 29$) and 43.3% in 2HIT-condition ($n = 30$), suggesting higher resilience to combined stress in females (Fig. 1b). While female mice received a modified protocol using male urine for generating 2HIT female mice due to inability to undergo RSDS from male aggressor ICR mice (Methods), the number of insistent chases and attacks were comparable to male offspring (Supplementary Fig. 1p, q).

To assess the brain immune environment in single-hit and 2HIT models through development, we counted microglia in the brain using Iba1 immunostaining (Fig. 1c-e and Supplementary Fig. 2–4). Figure 1c shows microglial density of male Control and 2HIT-susceptible (2HIT sus) mice brains. We investigated both male and female brain regions at 2-, 5-, and 9-week-old under different stress conditions. Our custom cell-counting program ensured stable cell counts (Methods, Supplementary Fig. 3). Iba1(+) microglia density in the cerebellar cortex, cerebellar nuclei, and ventral tegmental areas (VTA) of male 2HIT mice increased significantly at 5 weeks (Fig. 1d and Supplementary Fig. 4a, Male), while 2HIT stresses mainly exhibited microglia increase in the cerebellum and medial prefrontal cortex (mPFC) at 9 weeks. In contrast, microglia density did not significantly change in the hippocampus (dorsal dentate gyrus), VTA, and periaqueductal gray (PAG) at 9 weeks of age. In females, 2HIT sus cerebellar cortex also showed increased microglia similar to males, whereas both male and female resilient (2HIT res) mice showed no differences (Fig. 1d, e and Supplementary Fig. 4). Findings in BALB/c mice indicated that 2HIT stress-induced increase in cerebellar microglia was mouse strain-independent (Supplementary Fig. 5). Co-labeling with Ki-67, a cell proliferation marker, showed a marked increase in Ki-67(+) microglia density in the cerebellum of both 5- and 9-week-old 2HIT male mice (Fig. 2a–c). Either RSDS-susceptible (RSDS sus) or MIA weakly showed Ki-67 increase. The increased proportion of Ki-67(+) microglia after second-hit stress suggests that not only the total number of microglia increased but also their proliferation advanced in the 2HIT cerebellum (Fig. 2d). Co-labeling with cleaved fragment of Caspase 3 (Clv-Caspase3), an apoptosis marker, showed an increase in Clv-Caspase3(+) microglia[30] in the cerebellum of 9-week-old 2HIT males (Fig. 2e-g) but not at 5 weeks or in other regions. Neither RSDS nor MIA showed any increase in Clv-Caspase3(+) microglia, suggesting insufficient to cause their apoptosis. The increased Clv-Caspase3(+) microglia after second hit stress suggests their cell death advanced (Fig. 2h). Together, these results suggest increased microglial turnover in the 2HIT cerebellum.

For quantifying morphological differences, we assessed the microglial processes. 3D reconstruction and Sholl analysis of the Iba1(+) microglia in male mice showed a significant reduction in their branching, particularly in the cerebellar cortex and nuclei, depending on the stress conditioning (Fig. 3a-d and Supplementary Fig. 6-8). Either RSDS sus or MIA sufficiently changed cerebellar microglial morphology, while 2HIT stress caused further alterations. In contrast, we found microglia blunting in response to RSDS in VTA, which was reverted by second hit stress (Fig. 3c), suggesting regional differences in male mice. Female data also indicate morphological alterations in response to 2HIT stress (Fig. 3d). Microglial morphology in resilient mice of both sexes remained unaffected (Fig. 3c-f). Accordingly, 2HIT stress responses of microglia appear in the cerebellum. Recent observation in MIA mice by poly(I:C) administration at E9.5 revealed alteration of microglia morphology in the ventral striatum[31]. Our finding suggests that the later timing of MIA conditioning at E12.5 and additional peripubertal RSDS caused the regional difference.

The replacement of microglia prevents the increase and morphological changes of microglia

Given stress synergy leads to the distribution and transformation of reactive microglia in the brain, removing phenotypic microglia and replenishing a new population may reset the immune environment. To investigate if primed microglia by MIA change their number and branching in response to defeat stress at 4 weeks, we depleted microglia by CSF1R inhibition during RSDS conditioning (Fig. 1a). Repopulation of microglia primarily occurs through proliferation of the remaining subpopulation[45]. We therefore

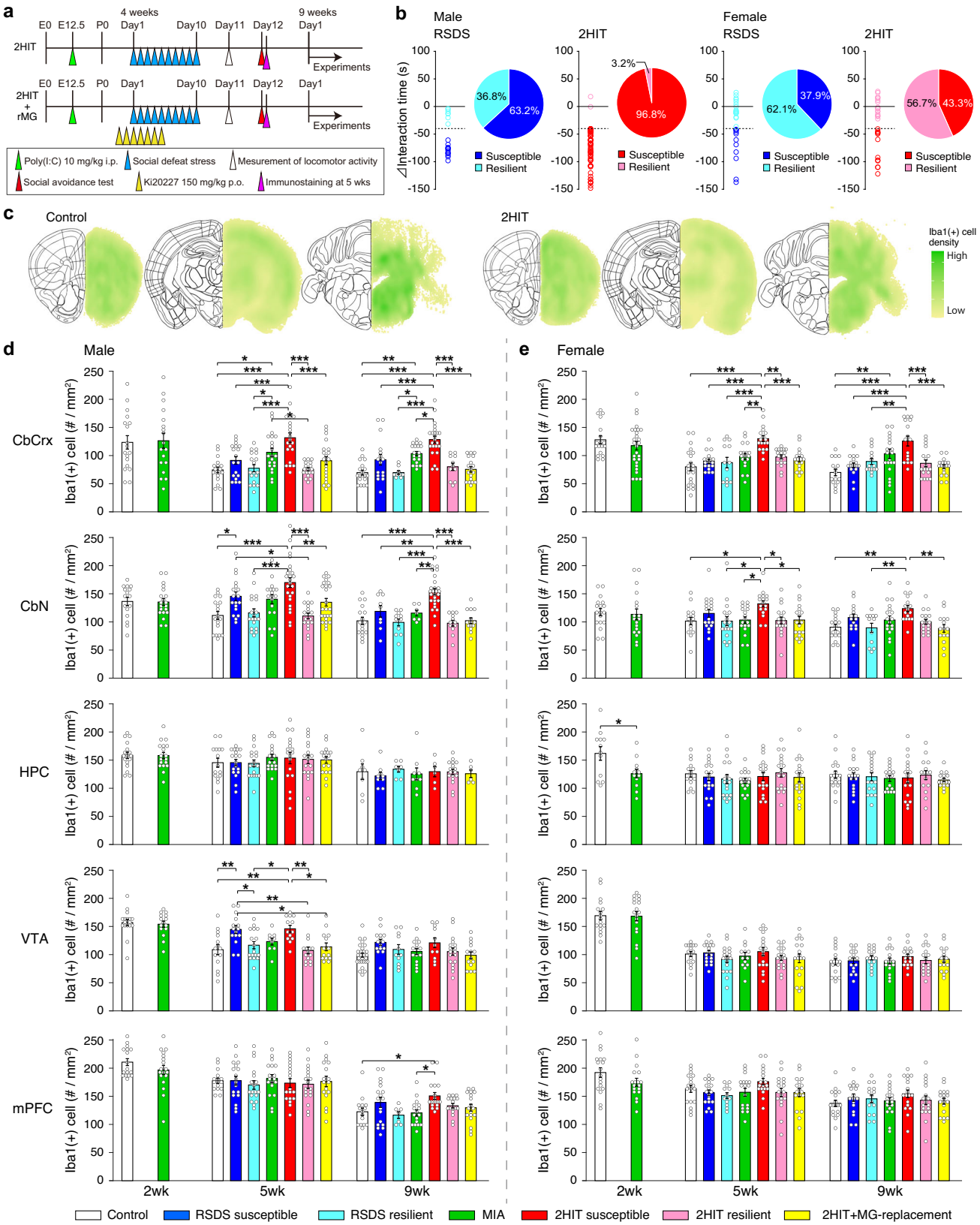

depleted microglia across the brain once (Supplementary Fig. 1r, s). We found that changes of the number of microglia, Ki-67(+) and Clv-Caspase3(+) microglia density, and their branching, in response to 2HIT stress, reverted to the control level after four weeks of repopulation (Figs. 1d, e, 2, 3e, f, Supplementary Figs. 2, 6, and 7; 2HIT+microglia-replacement (rMG)). These results suggest that a combination of inflammatory stress along a development spanning early puberty initiates an inflammatory milieu in 2HIT animals and the microglia replacement resets the tuned state.

Fig. 1 | 2HIT stress susceptibility associated with sex differences in mice is underlain by increased cerebellar microglia. a Experimental timeline for 2HIT mouse generation. We applied poly(I:C) to the pregnant mothers at embryonic day (E)12.5 as maternal immune activation (MIA). Repeated social defeat stress (RSDS) was exposed at 4 weeks old for 10 days. For 2HIT-microglia replacement (2HIT +rMG), a CSF1R inhibitor, Ki20227 was administered from 2 days before exposure to RSDS for seven days to deplete existing microglia. **b** The higher stress susceptibility in male 2HIT. The time difference in the zone with or without a stressor mouse during the social avoidance test (left plot) and the proportion of male and female mice susceptible (sus) and resilient (res) to RSDS (right pie charts) are shown. **c** A density increase of cerebellar Iba1(+)-microglia. Normalized density plots of coronal brain slices containing medial prefrontal cortex (mPFC), hippocampus (HPC), and cerebellum of male Control ($n = 3$) and 2HIT susceptible ($n = 3$) are shown. Cell density of Iba1(+) microglia. Bar graphs of the cerebellar cortex (CbCrx), cerebellar nuclei (CbN), HPC, ventral tegmental areas (VTA), and mPFC in the experimental C57BL/6N mouse groups (Control, RSDS susceptible (sus), RSDS resilient (res), MIA, 2HIT sus, 2HIT res, and 2HIT+rMG) across sex (male (**d**) and female (**e**)) and developmental periods (2-, 5-, and 9-weeks of age). The microglia density was restored after 1 week (at 5 weeks old) and four weeks (at 9 weeks old) after CSF1R inhibitor Ki20227 treatment. Data are shown as mean ± SEM in (**d**) and (**e**). $^{*}p < 0.05$, $^{**}p < 0.01$, and $^{***}p < 0.001$, one-way ANOVA with *multiple comparisons* using the Tukey-Kramer method.

The emergence of stress-associated microglia/macrophages in the 2HIT cerebellum

Recent studies have highlighted the diversity in transcript expression and functional heterogeneity of microglia[22–25], though specific characteristics based on multiple protein expressions have yet to be fully explored. Next, we sought the molecular signature and cell association in the single- and double-hit brains, using imaging mass cytometry (IMC) (Fig. 4 and Supplementary Fig. 9) and single-cell proteomics (Fig. 5 and Supplementary Figs. 10-16). IMC with designed 24-antibody markers and standard Iridium (Ir)-intercalators to FFPE sections (Methods) from stress-model brains successively yielded highly multiplexed images of different microglia/macrophage subpopulations, neurons, astrocytes, blood–brain barrier (BBB), pericytes, and vasculatures, with 1-μm precision (Fig. 4d and Supplementary Figs. 9,10). Notably, we found unique immune cells expressing distinct molecules, such as MHC class II, interleukin 6 signal transducer (IL6ST) (i.e., gp130), TREM2, TGFBR2, APOE, and MMP-9, in the cerebellar cortex, dentate nucleus (DN), fastigial nucleus (FN), and medial vestibular nuclei (MVN) (Fig. 4d and Supplementary Fig. 9a-d). We termed these immune cells stress-associated microglia/macrophages (SAMs) by multiple-protein expression with IMC. MHC-class II(+) immune cells were scarcely found in other brain areas (Fig. 4e, f). Disease-associated microglia (DAM) was previously identified in transcriptome studies on Alzheimer's disease[26,46–48] and other neurodegenerative diseases, including amyotrophic lateral sclerosis, tauopathy, and multiple sclerosis[49–52]. However, this study is the first to apply IMC to stress models and identify distinct microglia/macrophages at the proteomics. We also found SAM-marker-positive cells in our human postmortem brain samples with neurodegenerative disease in the IMC (Supplementary Fig. 9e). The 2HIT SAM puncta have distinct cell size and spatial localization. Classification based on manual measurement suggests two populations by puncta diameters among MHC-class II(+) immune cell punctum in both the cortex and nucleus: small ($\Phi < 10$ μm, 87.2% of the total 78 cell punctum) and large ($\Phi > 10$ μm, 12.8% of the total) populations (Fig. 4e-h). SAMs were closely associated with claudin-5-positive vasculatures and the ventricular surface (Fig. 4i), as described below. These results indicate spatially distinct subsets of microglia/macrophages in 2HIT brains at the multiple-protein expression level.

Cellular and molecular signature via IL-6 and TGF-β pathways revealed by the single-cell proteomics

Proliferated parenchymal or border-associated microglia likely contribute to SAM emergence[24,26,28,46]. Yet, the spatial proteomic signature and the transitional states in 2HIT models are elusive. We performed cell segmentation and spatial single-cell proteomics of multiplexed imaging data (Supplementary Fig. 12 and Fig. 5a-f), using Ir-images to segment cellular nuclei and measuring IMC signal intensity (Methods). For clustering, we analyzed signals from 24 markers: αSMA, Olig2, IBA1, Sall1, MMP-9, MAP2, Lyve1, TGFBR2, Claudin-5, GFAP, IL6ST/gp130, IL-6, AQP4, TMEM119, Caspase-1, PDGFR beta, Ki67, TGF-β1, IL-17RA, TREM2, CX3CR1, MHC-class II, APOE, and IL-17. Supplementary Fig. 10 and 13 show representative marker-positive cells and signal intensity profiles of the marker-molecules. We identified 4284 and 5895 cells in the Control and 2HIT cerebellar cortex, respectively (Methods). Cell segmentation of Control and 2HIT revealed cell-type specific clusters (12 clusters in Control and 14 clusters in 2HIT) in the cerebellar cortex (Supplementary Fig. 12a [Control] and Fig. 5a [2HIT]). Single-cell clustering using tSNE showed clusters of distinct cell populations based on cell-type-specific markers (Supplementary Fig. 12b-d [Control] and Fig. 5b-d [2HIT]). In control cerebellar cortex, by using 24-marker signal intensity and the localization pattern, we annotated 12 clusters, including granule-cell layer neurons, molecular layer interneurons, immune cells, astrocytes, vasculatures, pericytes, and oligodendrocytes (Supplementary Fig. 12c). Immune cells were identified by Iba1, Sall1, and CX3CR1 expression, and neurons were identified by MAP2 expression and limited immune-cell marker expression. Due to the 4-μm IMC thickness, large cells like Purkinje cells were not fully detected. In Control immune cells, TMEM119, CX3CR1, and IL-17RA are prominent, whereas there is less expression of IL6ST, TGFBR2, TREM2, MHC-class II, and MMP9 (Supplementary Fig. 12b-d). In contrast, the 2HIT cerebellar cortex demonstrated distinct immune-cell clusters characterized by IL6ST, TGFBR2, TREM2, MHC-class II, MMP9, APOE, Ki67, TGF-β1, Caspase-1, and Lyve1 expression (clusters 12 and 14) (Fig. 5b-d), with clusters 12 and 14 composing 2.2% and 0.9% of cells, respectively. Ki-67 expression is highest in Cluster 12 in 2HIT cerebellar cortex, representing up to 6.1% of immune cells (see also Fig. 2c). No SAM was found in the single-cell spatial proteomics of RSDS sus and MIA cerebellum (Supplementary Fig. 12e-h [RSDS] and 12i-l [MIA]). Thus, a 2HIT stress-associated cluster is present in the cerebellum. The localization of spatially segmented clusters corresponds to the location of SAMs in the superimposed images of multiplexed staining (Fig. 5a and Supplementary Fig. 14a). Interestingly, Clusters 12 and 14 are located near each other, with SAM-puncta in Cluster 12 (Supplementary Fig. 14a, squares). Accordingly, we annotated Cluster 12 as SAM and Cluster 14, marked by Lyve1, as border-associated macrophages (BAM[28,46]) via IMC.

To determine whether the different protein-expression phenographs result from individual differentiation or consecutive steps in stress synergy, we analyzed cell transitions[46,48] using IMC expression data and PHATE mapping (Methods) (Supplementary Fig. 14b-e). In 2HIT, but not Control, immune cells, composing different clusters, formed in a continuous trajectory, indicating in-series differentiation of microglia/macrophage in the cerebellum (Supplementary Fig. 14c). The PHATE transition entropy predicted a directional cell transition or differentiation (an arrow in Supplementary Fig. 14c). Cluster 14 did not align with the pathway. Therefore, we considered Cluster 12 in 2HIT as the mature SAM. Cluster 6 (immune cells) has a molecular signature in the transition state from homeostatic state to SAM cluster and was identified as a potential progenitor (proSAMs). RSDS datasets suggested a consecutive transition from naïve microglia to proSAMs, while the transition was minor in MIA (Supplementary Fig. 14d, e). Together, we postulated that MIA primes naïve microglia and proSAMs, and the subsequent RSDS facilitates their transitions into mature SAMs.

To explore spatial links between clusters, we performed a pairwise distance analysis of cells (Supplementary Figs. 15 and 16). In Control, Cluster 10 (Vasculature) and Cluster 11 (Pericytes) were in proximity, whereas in 2HIT, the pairwise distance was significantly close between Cluster 10 (Vasculature), Cluster 12 (SAM), and Cluster 14 (BAM). Results

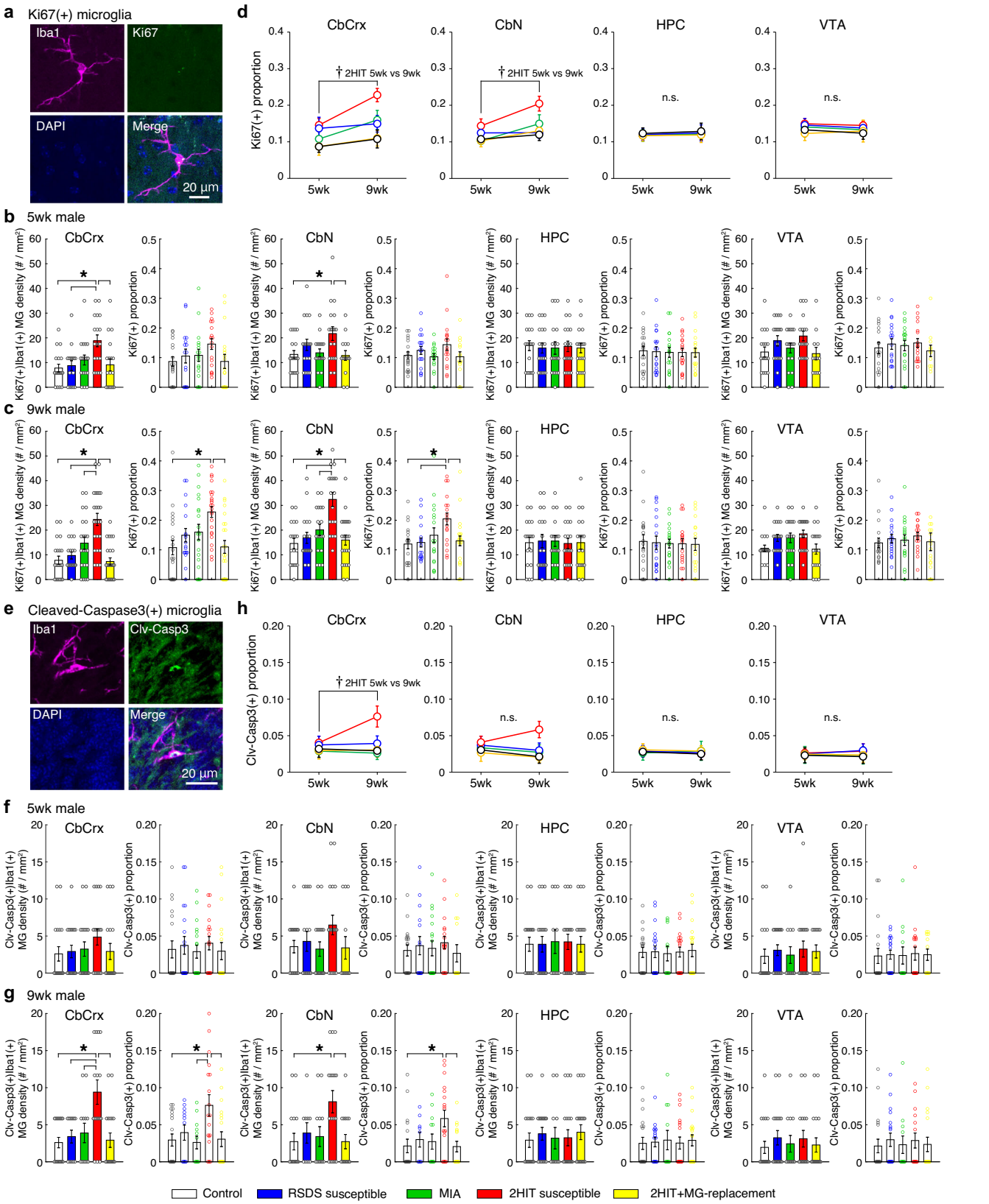

suggest that SAMs and BAMs are closely localized to the vasculature in the 2HIT cerebellum, consistent with findings in Fig. 4i.

Mixture analysis of immune cell datasets of Control and 2HIT also provides a distinct cluster 13 with the SAM-associated protein expression pattern (Fig. 5e, f), assumingly reflecting the SAM gene expression[24,26,47,50]. A volcano plot comparing the expression patterns of immune cells and SAM showed elevated expression of TGF-β1, APOE, IL-6, and TREM2 (Fig. 5f), suggesting the promotion of molecular signaling pathways. However, due to the abundance of granule cells, there is an experimental limitation causing overestimation.

Fig. 2 | Increased microglial turnover in the cerebellum following 2HIT stress exposure. a Representative immunostaining of Ki67(+) microglia. Images show Iba-1(+) microglia, DAPI-stained nuclei, and cell proliferation marker Ki67 expression in a male mouse. **b**, **c** Bar graphs showing the density and proportion of Ki67(+) microglia. Data from 5- (**b**) and 9- (**c**) week-old male Control, RSDS susceptible (RSDS sus), MIA, 2HIT susceptible (2HIT sus), and 2HIT+microglia replacement (rMG) groups are presented across the cerebellar cortex (CbCrx), cerebellar nuclei (CbN), hippocampus (HPC), and ventral tegmental area (VTA) (mean ± SEM). **d** Time course of the Ki67(+) microglia proportion. The proportion of Ki67(+) microglia in male is plotted at 5 and 9 weeks of age. The proportion of CbCrx Ki67(+) microglia in the 2HIT sus group has increased significantly at 9 weeks under stress conditions than at 5 weeks. **e** Representative immunostaining of cleaved Caspase 3 (clv-Casp3)-positive microglia. Images show Iba-1(+) microglia, DAPI-stained nuclei, and apoptosis marker clv-Casp3 expression in a male mouse. Bar graphs showing the density and proportion of clv-Casp3(+) microglia. Data from 5- (**f**) and 9- (**g**) week-old male Control, RSDS sus, MIA, 2HIT sus, and 2HIT +rMG groups are presented across CbCrx, CbN, HPC, and VTA (mean ± SEM). **h** Time course of the clv-Casp3(+) microglia proportion. The proportion of clv-Casp3(+) microglia in male is plotted at 5 and 9 weeks of age. The proportion of CbCrx clv-Casp3(+) microglia in the 2HIT sus group has increased significantly at 9 weeks under stress conditions than at 5 weeks. * indicates significance by one-way ANOVA with multiple comparisons (Tukey-Kramer method) ($p < 0.05$), and † indicates significance by two-sample unpaired Student's t-test ($p < 0.05$).

Finally, we confirmed SAM markers (Iba-1, TREM2, MHC-class II) with conventional triple immunostaining (Fig. 5g-l). In the male 2HIT cerebellar cortex, 10.4 ± 2.7% of Iba-1(+) microglia were double-marker positive (Fig. 5i), similar to IMC findings. Female 2HIT sus also had 5.5 ± 1.5% marker positive microglia in the cerebellum (Fig. 5l), dominantly, but not in other regions or both male and female resilient mice. Immunohistochemistry images also corroborate the blunted morphology of 2HIT (Fig. 5g, j) and the remedy of SAM-marker positive microglia by microglia replacement in both sexes (2HIT+rMG) (Fig. 5h, i, k, and l).

Purkinje cell loss in the 2HIT cerebellum

Next, we asked if the increase in reactive microglia links to disruptions of the neuronal circuit in stress accumulation, leading to cerebellar dysfunction. Since the loss of 20–33% of Purkinje cells in the MIA-exposed animals was previously reported[53], we investigated the possibility of neural loss in the cerebellar lobules by the accumulative stress (Fig. 6 and Supplementary Fig. 17 and 18). First, we found a prominent reduction in Calbindin(+) Purkinje cells in lobule VIa-VIb of the 2HIT cerebellum (Fig. 6a, b). The number of Purkinje cells decreased by 38.4% in lobule VIa-VIb, spanning to the entire cortex of the male 2HIT (lobules II–IV and IX–X, Fig. 6b), suggesting a promotion of Purkinje-cell loss in the stress-exposed cerebellum compared to MIA solely. At 9-week-old, Purkinje cell loss was significantly increased than at 5-week-old (Supplementary Fig. 18). Female MIA and 2HIT also showed a 28.8% and 38.9% reduction in lobule VIa-VIb Purkinje cells, respectively (Fig. 6g). Although the neurodegeneration by MIA was progressive in the course of development[53], the second hit RSDS accelerated the neuron loss (Fig. 6b, g and Supplementary Fig. 18). In contrast, Calbindin(+) interneurons in mPFC were comparable across stress conditions and sexes (Supplementary Fig. 19), implying cerebellum-specific disruption. Notably, the microglia replacement ameliorated the cerebellar neurodegeneration in both sexes (Fig. 6a, b, f, g, 2HIT+rMG), suggesting the involvement of microglia reactivity.

In identical cerebellar cortical slices, the density of Calbindin(+) Purkinje-cell axons decreased, and the density of Iba1(+) microglia increased, respectively (Fig. 6c, d, h, i). Principle component analysis (PCA) showed a distinct separation of 2HIT group (Fig. 6e [male] and 6j [female]). Multivariate Analysis of Variance (MANOVA) ($^*p < 1.6 \times 10^{-11}$ and 6.0×10^{-10}, respectively) of the three measurements across Control, 2HIT sus, and 2HIT+rMG indicates a strong correlation between Purkinje cell loss, the axon decrease, and microglia increase. Therefore, microglial reactivity in response to 2HIT stress is implicated in the Purkinje cell loss and axon degeneration[41,43].

Inflammatory stress synergy reduces intrinsic excitability

How do reactive microglia alter neurophysiological properties in stress accumulation models? To determine the independence or the additivity of multiple developmental stresses with MIA and RSDS sus in the neurophysiological properties of Purkinje neurons, we first examined the firing of action potentials evoked by depolarization step-pulses under suppression of synaptic transmission. In Fig. 7a-o, the firing frequency of Purkinje cells was reduced in male MIA, 2HIT sus but not in male RSDS sus. Our results on male MIA and 2HIT sus are reminiscent of the finding that the intrinsic excitability of Purkinje cells was reduced in another autism spectrum disorder (ASD) model mice[36]. Next, waveform analyses of an action potential showed an increase in input resistance, half width (i.e., FWHM), 10–90% rise time of action potential in MIA and 2HIT sus Purkinje cells, suggesting the modulation of voltage-gated K^+ and Na^+ channels, which corroborated the reduced intrinsic excitability (hypoexcitability) (Fig. 7d-o). Female 2HIT sus Purkinje cells also showed changes in action potential (Fig. 7p, q) and intrinsic membrane excitability properties (Fig. 7r-ac). Again, female 2HIT res Purkinje cells were comparable to Control. Therefore, these results indicate that the intrinsic excitability of Purkinje cells is lower in 2HIT sus animals. Incidentally, firing frequency and action-potential waveform were comparable between Control and 2HIT sus mPFC layer 5 pyramidal neurons (Supplementary Fig. 20).

To investigate if the reactive microglia by 2HIT conditioning modulated the intrinsic excitability of Purkinje cells, we depleted microglia during 2HIT conditioning and performed a patch-clamp after recovery at 9 weeks of age. Then, the firing frequency of action potential reverted to the control level (Fig. 7, 2HIT+rMG). The results indicate that the 2HIT-stress-induced inflammatory milieu disrupts the membrane properties of the cerebellar neurons and reduces their excitability.

2HIT stress insults during the developmental period induce functional dysconnectivity and behavioral anomalies

Ejection impairment of Purkinje-neuron action potentials (Fig. 7) and reduced axon density (Fig. 6c, h) may disrupt long-range neural transmission in vivo. Next, we performed resting-state fMRI to parcellate pathways with malfunction among four conditions. Figure 8a shows correlation matrices of the blood-oxygen-level dependent (BOLD) signals across 90 brain seeds (Supplementary Data 1). Z-scores of Pearson correlation coefficient as the index of functional connectivity revealed significantly decreased correlations between the cerebellum (cerebellar cortex and nucleus), midbrain (VTA and PAG), and prefrontal cortex (mPFC, cingulate, and primary motor cortex) in stress model mice (Fig. 8a). From the connectivity matrices, we generated network models, visualizing interaction networks at significant level (Fig. 8b), which show specific reductions in 2HIT at cerebellar cortex, nuclei, pons, VTA, PAG, insular, and mPFC regions (Fig. 8c). Thus, the cerebellum-involved pathways are impaired in the resting state.

Since Purkinje cell axon density decreased in 2HIT sus mice (Fig. 6c, h), we investigated axon structure and myelin sheath changes via electron microscopy. In 2HIT sus, both axon diameter and g-ratio were significantly reduced in the cerebellar dentate nucleus (Fig. 8d), suggesting a reduction in thick-caliber myelinated axons compared to controls (Fig. 8d-f). Similar results were obtained in VTA, a projection target from the dentate nuclei, while PAG and mPFC showed no diameter or g-ratio changes. Next, we tested if microglia replacement could restore 2HIT microstructural deficits (Supplementary Fig. 21). Microglia replacement in the 2HIT brain did not significantly alter axon diameter or g-ratio, suggesting limited microglia involvement in cerebellar axon shrinkage recovery (Supplementary Fig. 21). Considering that oligodendrocyte differentiation and axon diameter in the developing male cerebellum underlie the social behavior[54], our results

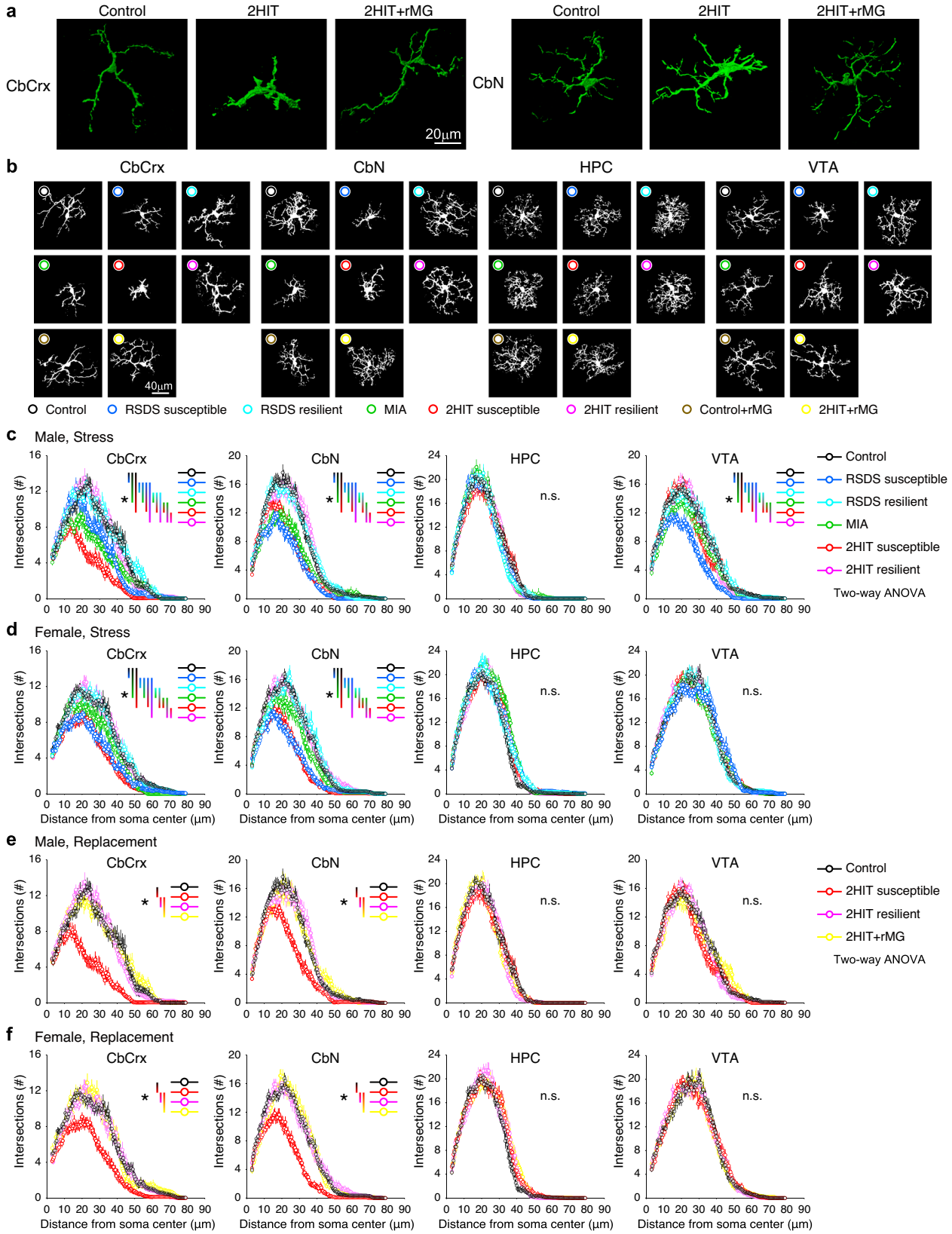

suggest the disruption of the axon transduction in the cerebellum-involved networks of 2HIT brains.

Hypoactivity of the cerebellum and disruption of its associated pathways may lead to behavioral anomalies. We conducted a battery test of mouse behaviors in male and female Control, RSDS sus/res, MIA, 2HIT sus/res, Control+rMG, and 2HIT+rMG groups, assessing social avoidance, open field, elevated plus maze, 3-chamber, social dominance, marble burying, novel object recognition, and prepulse inhibition (PPI) (Fig. 9a-j, 9n-t). We further tested for motor coordination on the rotarod and footprint stride analysis (Fig. 9k-m, 9u-w). Multiple behavioral deficits appeared across stress

Fig. 3 | Morphological blunting of microglia in the 2HIT stress-exposed brain. **a** 3D-reconstructed images of cerebellar microglia from Control, 2HIT, and 2HIT after microglia-replacement (2HIT+rMG) male animals. Representative microglia from the cerebellar cortex (CbCrx) and nuclei (CbN) are shown. **b** Representative microglial morphology stacks from CbCrx, CbN, hippocampus (HPC), and ventral tegmental areas (VTA) of male Control, RSDS-susceptible (RSDS sus), RSDS-resilient (RSDS res), MIA, 2HIT-susceptible (2HIT sus), 2HIT-resilient (2HIT res), Control after microglia-replacement (Control+rMG), and 2HIT+rMG animals. Sholl analysis of stress-conditioned microglia (Control, RSDS sus, RSDS res, MIA, 2HIT sus, and 2HIT res) in different brain regions in male (**c**) and female (**d**) mice, showing interaction counts against concentric circles. Data are presented as mean ± SEM. Two-way ANOVA group × distance, interactions: Cbcr, $F(500, 11009) = 2.58$, $p < 0.0001$; CbN, $F(500, 13231) = 3.07$, $p < 0.0001$; VTA, $F(500, 12726) = 1.32$, $p < 0.0001$, in male (**c**). Two-way ANOVA group × distance, interactions: Cbcr, $F(500, 16362) = 1.23$, $p < 0.0005$; CbN, $F(500, 15352) = 2.22$, $p < 0.0001$, in female (**d**). *$p < 0.0001$, *multiple comparisons* using the Bonferroni method. A significant interaction effect was observed between distance and stress conditions. Sholl analysis of microglia across microglia-replacement condition (Control, 2HIT sus, 2HIT res, and 2HIT+rMG) in different brain regions in male (**e**) and female (**f**) mice. Two-way ANOVA group × distance, interaction: Cbcr, $F(300, 8686) = 2.53$, $p < 0.0001$; CbN, $F(300, 9797) = 2.91$, $p < 0.0001$, in male (**e**). Two-way ANOVA group × distance, interactions: Cbcr, $F(300, 10201) = 1.58$, $p < 0.0001$; CbN, $F(300, 9999) = 2.47$, $p < 0.0001$, in female (**f**). There was a significant interaction effect between distance and stress conditions (*$p < 0.0001$). The results suggest reduced process arborization of cerebellar and VTA microglia in stress models of both sexes, with improvements observed after microglia replacement. See also Supplementary Figs. 7 and 8.

model groups of RSDS sus, MIA, and 2HIT sus (Fig. 9). In social-avoidance tests RSDS and 2HIT sus models showed pronounced aversive responses, unlike Control and MIA (Fig. 9a). In Fig. 9j, reduced PPI in MIA and 2HIT sus males indicated less habituation to the startle response, representing impaired sensorimotor gating as schizophrenic-like stress responses. Despite normal auditory responses to weak auditory stimulation, 2HIT sus males exhibited heightened startle responses to loud sounds (Supplementary Fig. 22). The timing of RSDS also affected behavioral outcomes since animals exposed to RSDS at 9 weeks old showed milder anomalies (Supplementary Figs. 1k-o and 23). Further, the motor performance tests revealed clear motor coordination deficits in 2HIT sus and RSDS sus, though without ataxia in both sexes (Fig. 9k-m, 9u-w). Female 2HIT sus also showed multiple deficits in behaviors with differences from male phenotypes in OF, EPM, and MB tests, representing higher anxiety, while female 2HIT res was comparable to female Control (Fig. 9n-t). Altogether, our findings suggest synergistic effects of single-hit (RSDS and MIA) and 2HIT models on sociability, exploratory behavior, anxiety, stereotypy, compulsive behavior, episodic-like memory, and startle reflex (Fig. 9x, y). Sex differences in the behaviors of 2HIT sus males and females suggest increased anxiety and sociability in females compared to males (Fig. 9z). Results allow a scenario that motor dyscoordination in stress-exposed animals may impact higher-order cognitive behaviors.

Finally, we attempted to restore these behavioral anomalies in 2HIT model via microglia replacement. As expected, microglia replacement led to behavioral recovery in both sexes (Fig. 9, 2HIT+rMG), consistent with reduced microglial reactivity and stress-induced neural disruptions.

Cerebellum-specific microglia replacement suffices for 2HIT phenotype prevention

To assess microglia reactivity in the cerebellum, we performed cerebellum-specific depletion of microglia and examined the consequences. To remove microglia in the cerebellum specifically, we injected clodronate disodium salt (CDS) into the peripheral vermis of male mice (total 1.2 µL vol. of 50 mg/ml CDS) (Fig. 10a). We then counted the number of microglia one, five, and thirty days after injection, comparing CDS and phosphate-buffered saline (PBS) injection. Microglia were significantly reduced at 5 days post-injection (dpi) and returned to control levels at 30 dpi (Fig. 10b, c). Figure 10c shows microglia density across six brain regions at 5 dpi, confirming effective cerebellum-specific depletion. Then, we injected CDS one day before RSDS (Fig. 10d). At nine weeks of age, the number of cerebellar microglia returned to control levels (Fig. 10e), while 2HIT mPFC microglia remained to show a slight increase (119.2%). The density of MHC class II(+) TREM2(+) was scarce in the cerebellum (Fig. 10f, 2HIT + CDS), suggesting limited SAM generation. Cerebellum-specific microglia depletion prevented Purkinje cell loss induced by the stress combination (Fig. 10g). Electrophysiological recording indicated Purkinje cell firing frequency (Fig. 10h, i) and action-potential waveform parameters (Fig. 10j-p) were restored to PBS-injected Control levels, showing improvement from 2HIT levels. Moreover, the behavior test battery demonstrated the remedy in cognitive-affective behaviors and motor coordination following CDS injection (Fig. 10q-z). These results indicate that cerebellar microglia replacement successfully mitigates 2HIT phenotypes.

Discussion

The "two-hit hypothesis" was originally proposed to explain the diathesis-stresses model of psychoses via a combination of genetic and environmental factors[15–17], with the genetic abnormality considered epigenetic. While our study primarily focuses on the accumulation of environmental stresses, MIA is known to induce epigenetic changes and microglia blunting[31,55,56]. The short and mild SDS conditioning resulted in epigenetic regulation and synaptic transmission modulation, although transcript expression did not necessarily correlate with neural functions[57]. Microglia density (Fig. 1d,e) and turnover (Fig. 2) were increased in the cerebellum of susceptible mice, suggesting that microglia number—and possibly their reactivity—correlate with susceptibility in 2HIT mice. In this study, we generated female 2HIT mice for the first time, to our knowledge. The females were less vulnerable to stress accumulation than males; 56.7% of female mice were resilient, compared to only 3.2% of male mice (Fig. 1b). Our female mice exhibited greater resilience to RSDS compared to the males, indicating potential sex differences in vulnerability or responsiveness (Fig. 1b,d,e). VanRyzin et al. (2019) demonstrated sex differences in the microglia features (e.g., phagocytosis) in the amygdala during early development, affecting social behavior consequences[29]. Given that susceptibility to 2HIT stress correlated with cerebellar microglia (Figs. 1, 2, and 3), it is possible that cerebellar microglia exhibit sex differences in 2HIT stress responsiveness, as represented by reactive microglia[8,34]. Sexual differences in the cerebellum have been rarely reported; thus, it is of particular interest given the association between this region and behavioral phenotypes linked to stress-associated disorders, which often display a strong male bias. However, the mechanism underlying sex differences is yet fully elucidated; further investigation is required.

MIA alters microglial reactivity and induces a blunted, less-ramified morphology, often indicating heightened reactivity, via epigenetic regulation in the forebrain[32]. In our conditioning, Iba-1(+) microglia exhibited a less ramified shape in the 2HIT cerebellum but not in the hippocampus and VTA (Fig. 3b-d). MHC-class II(+) immune cells were found exclusively in the cerebellar cortex and nuclei in both sexes (Figs. 4d-f and 5g-l). The reactive microglia and mature SAM were characteristically localized around the cerebellum (Fig. 5h, i, k, l). The cerebellum was shown to entail characteristic microglial activity compared to other brain regions[27,55,58]. We consider the cerebellum vulnerable to MIA exposure at E12.5 in both sexes. In contrast, two key studies administered MIA on gestation day 9 and observed microglial alterations in the hippocampus[1] and forebrain[31]. The difference between the studies would be due to the timing of brain formation and microglia infiltration. At E7.5, the mouse cerebellar primordium emerges at the rostral lip of the fourth ventricle. Neuroepithelial cells generate the cerebellar neurons from around E10.5 to E13.5. Microglia originate from the yolk sac at E8.5 and infiltrate the parenchyma in a forebrain-to-hindbrain order. Therefore, the timing of MIA may determine which brain regions contain reactive microglia. The dose, duration, and quantity of poly(I:C) dsRNA fragments may also play a significant role[11]. Given that the

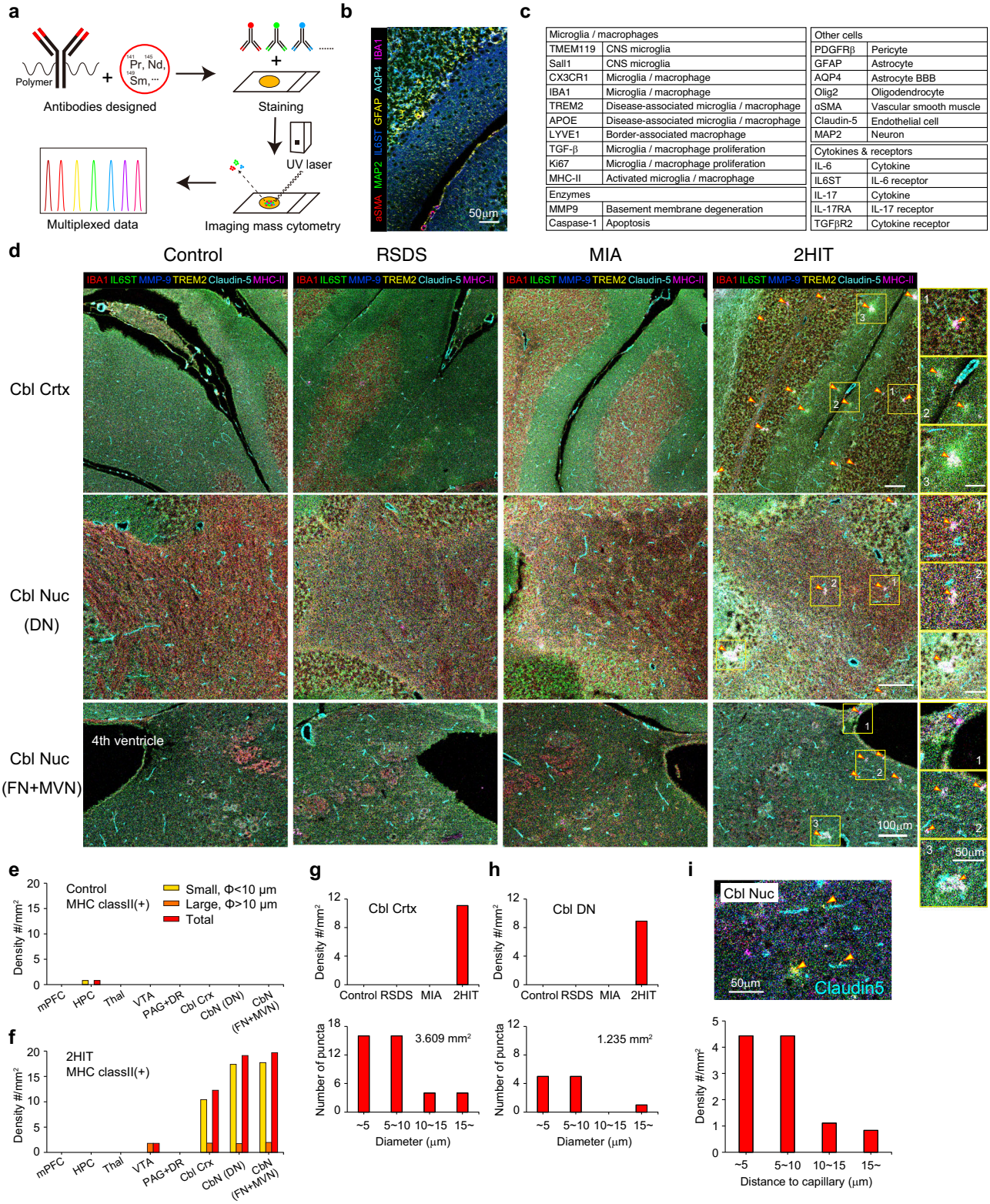

Fig. 4 | The emergence of stress-associated microglia/macrophages in 2HIT cerebellum and the near vasculature localization. a Schematic drawing of the imaging mass cytometry (IMC). Polymer-conjugated antibodies (Methods) are combined with labeling metals, which visualize the sharp spectrum by time of flight. **b** A multiplexed IMC image of the four-μm-thick cerebellar cortex. **c** Antibody-marker list. **d** IMC images obtained from cerebellar cortex (culmen and simple lobule), dentate nucleus (DN), and fastigial nucleus (FN)+medial vestibular nuclei (MVN) with IBA1, IL6ST/gp130, MMP9, TREM2, claudin-5, and MHC-class II markers. Yellow squares in 2HIT show representative 2HIT stress-associated puncta (arrowheads, Methods). Cerebellar cortex (Cbl Crtx). Cerebellar nuclei (Cbl Nuc). **e**,**f** An increase in MHC-class II(+) positive immune cells in the 2HIT cerebellum. The immune cell density was bar-graphed in different regions of Control and 2HIT. **g–i** An increase in stress-associated puncta in the cerebellum. The number of puncta was counted in two cerebellar regions (cerebellar cortex and dentate nucleus) of 2HIT. Density (# per millimeter square) and the histograms binned by diameter are shown. The total area of the cerebellar cortex (**g**) and dentate nucleus (**h**) are 3.609 and 1.235 mm^2, respectively. MHC-class II(+) microglia located near or colocalized to Claudin-5(+) vasculature (**i**). The histogram of density vs. distance to the capillary is shown at the bottom of (**i**).

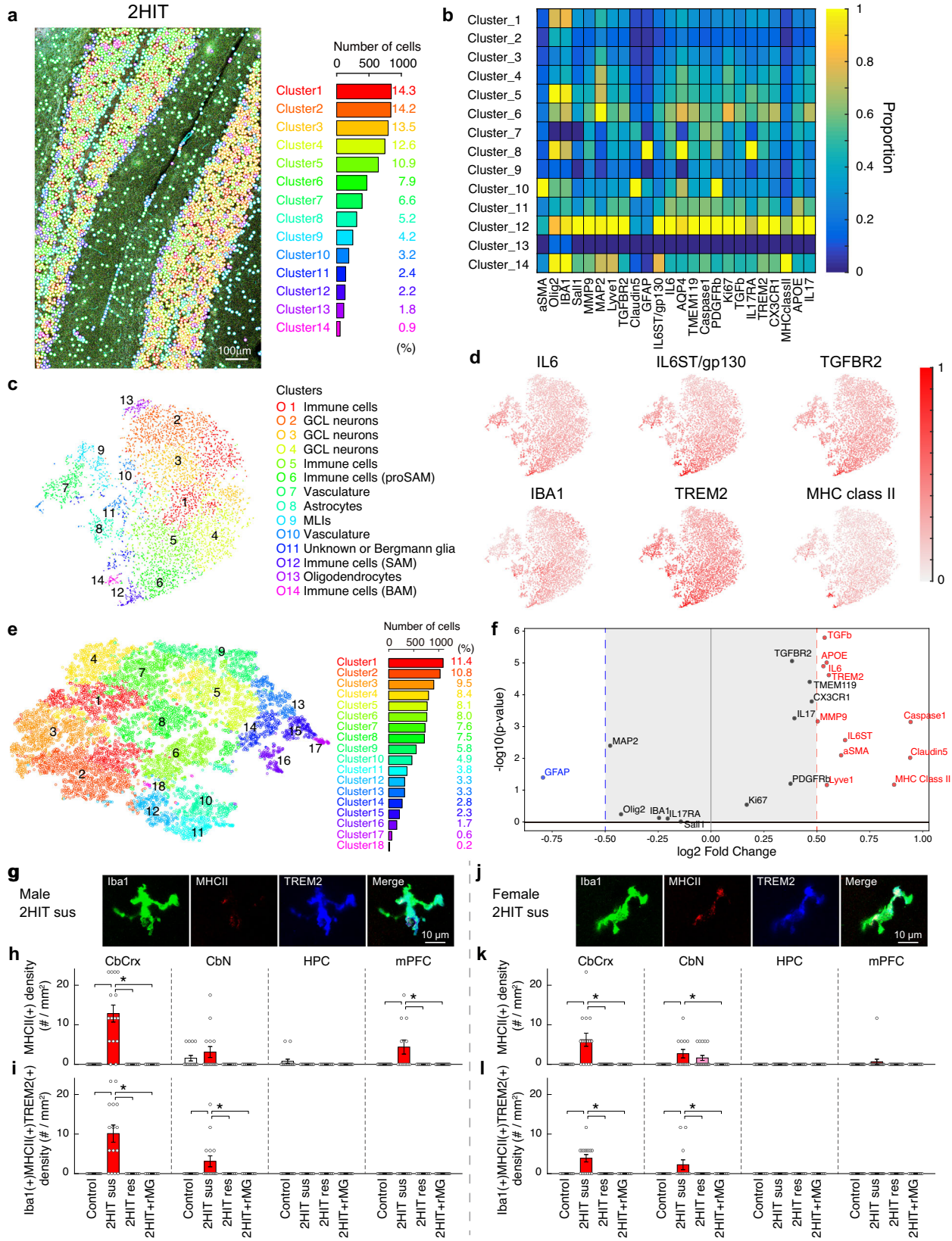

cerebellum is linked to symptoms of ASDs[36,37,44], our model may reflect the co-morbidity of the complex stress-associated disorders.

We hypothesize that the progenitors, proSAMs, were generated during the maturation following MIA exposure in 2HIT brains, and subsequent RSDS reactivates proSAMs and promotes their differentiation by expressing distinct factors. SAMs characteristically express signature proteins, such as TREM2, IL6ST, APOE, MMP9, and TGFBR2, which may lead to microglia proliferation and cerebellar pathophysiological disruption. As Smith et al.[9] described the increase in IL-6 in the MIA-exposed brain, we replicated the result of enhancement of IL-6-IL6ST signaling in the 2HIT cerebellum.

Fig. 5 | Single-cell spatial proteome analysis of the cerebellar cortex. **a** Classification of cell populations from IMC data. Single-cell segmentation superimposed with the IMC images of male 2HIT susceptible cerebellar cortex. **b** Heat map of the marker signal intensity by clusters. **c** tSNE plot and annotation of the clusters: immune cells, granule cell layer (GCL) neurons, molecular layer interneurons (MLIs), vasculature cells, astrocytes, oligodendrocytes, and unknown populations. In 2HIT, we termed cluster 6 progenitors of stress-associated microglia/macrophage (proSAM), cluster 12 SAM, and cluster 14 border-associated macrophage (BAM). BAM was annotated from the expression of Lyve1, MHC class II, and CX3CR1, and localization in the tissue. See also Supplementary Fig. 12. **d** Intensity plot of representative molecules in the tSNE maps. **e** tSNE plot of the mixture dataset of Control and 2HIT. The successful batch correction has effectively integrated the cells into the same clusters from both models, suggesting similar cell populations in the overall dataset. **f** Volcano plot showing the changes in the protein expression between immune cells and SAM cluster of the mixture dataset. Red-marked proteins have significantly higher expression in SAM compared to all the other immune cells. **g** Representative SAM images by immunohistochemistry, showing Iba1-, MHC class II-, TREM2-triple-positive-microglia in male 2HIT cerebellum. The density of MHC class II(+) immune cell (**h**) and Iba1-, MHC class II-, TREM2-triple-positive-cell (**i**) of cerebellar cortex (CbCrx), cerebellar nuclei (CbN), hippocampus (HPC), and medial prefrontal cortex (mPFC) in male Control, 2HIT sus, 2HIT res, and 2HIT +rMG. $*p < 0.05$, one-way ANOVA with *multiple comparisons*. **j** Representative SAM images by immunohistochemistry in female 2HIT cerebellum. The density of MHC class II(+) immune cell (**k**) and Iba1-, MHC class II-, TREM2-triple-positive-cell (**l**) in female Control, 2HIT sus, 2HIT res, and 2HIT+rMG. $*p < 0.05$, one-way ANOVA with *multiple comparisons* using the Tukey-Kramer method.

While IL-6 signaling is involved in immune cell differentiation, microglia repopulation, and lipid degradation[10,59], it may also affect different cellular functions. In this study, MIA and 2HIT models showed heightened expression of TGFBR2 and TGF-β1 in distinct immune cell clusters, which could drive TGFBR signaling, including Smad2/3, and promote microglia proliferation. Transcriptome studies predicted two-step process in DAM maturation in neurodegeneration models, driven by TREM2-independent and TREM2-dependent signalings[26]. Our SAM phenotype coincides with the transcript expression pattern, including TREM2, APOE, and TMEM119. While we observed distinct classification in SAM puncta size (Fig. 4d-h), their physiological roles remain unknown[47]. Our single-cell proteomics analysis predicted the transition to proSAMs and SAMs associated with IL6ST/gp130 signaling (Fig. 5b-d and Supplementary Fig. 14b-e). It has been shown that TREM2 interacts with lipids, including APOE[60–62], in neurodegenerative diseases and metabolic pathologies. Since mutations in TREM2 gene increase the risk for Alzheimer's disease[63] and other neurodegenerative disorders, TREM2-positive microglia are considered neuroprotective[64] in the field of neurodegenerative diseases. It is noteworthy that the expression differences between developing and senescent brains and the higher heterogeneity in human tissues.

According to Silvin et al.[47], in neurodegenerative diseases, DAMs are derived from naïve microglia in a TREM2-dependent manner, while disease inflammatory macrophage (DIM) originate from bone-marrow-monocytes and are TREM2-independent. In contrast, the expression pattern of Lyve1, MHC class II, and CX3CR1 (Fig. 5b) and their localization around vasculature (Fig. 4i and Supplementary Figs. 15, 16) may implicate the 2HIT SAM cluster exhibiting features of BAM[46,52]. We speculate that the second-hit stress, RSDS, disrupts vascular barriers via MMP9, caspase, and APOE, allowing inflammatory signals to infiltrate the parenchyma or vasculature surroundings[17]. This may drive the differentiation of proSAMs into mature SAMs with varying characteristics, too. SAMs could further promote BBB disruption through MMP9 expression and the breakdown of tight junction. However, it is still unknown how reactive microglia induces cell death of Purkinje cells, and further investigations are required.

In patients with ASD, cerebellar volume reduction and Purkinje cell hypoplasia were observed[65,66]. Schizophrenia patients show pathological atrophy of the cerebellar vermis and gray matter[67,68]. Our results from rodents revealed the low intrinsic excitability of Purkinje cells (Fig. 7). The analysis of the action potential waveform suggests modulation of voltage-dependent K^+ and Na^+ channel conductance in MIA and 2HIT sus Purkinje cells. These modulations could alter the conduction of synaptic currents along the dendrites, voltage-gated and Ca^{2+}-activated ion channels, their plasticity, and cerebellar output[38–40]. Purkinje-cell loss, axon degeneration, and reduced cerebellar output (Figs. 6 and 7) likely dysregulate the cerebellar nuclei, which project to the midbrain. The DN neurons project to VTA[69], and the FN neurons project to the ventrolateral PAG[70]. Degeneration of Purkinje cells and lowered cerebellar neural activity would decrease axonal conduction, which causes long-ranged brain-wide functional dysconnectivity and behavioral anomalies in the 2HIT model (Figs. 8 and 9). In the cerebellum of anesthetized rodents, increased pace-making spike activity of Purkinje cells and spontaneous local field potentials per se is insufficient to affect basal cerebral blood flow (CBF) and BOLD signals[71]. Rather, CBF is coupled with field potentials evoked by afferent fiber activation[71]. which may reflect the reduction of afferent fiber responsiveness in cerebellar Purkinje cells, similar to the reduction in synapse formation seen in adult PFC pyramidal neurons[72]. A recent study supports our consequence of the correlation between Purkinje cell hypoexcitability and brain-wide functional dysconnectivity[73], contrasting with findings from the acute cerebellar inflammation model[44].

According to Paolicelli et al., DAM is known to correlate with neurodegeneration, but DAM-related phenotypes should be understood in specified contexts[25]. DAM may include subpopulations, and their origin is not yet fully determined. We consider our 2HIT condition to express a spectrum of cerebellum-related cognitive dysfunction phenotypes. Both RSDS (e.g., trauma, bullying) and MIA (e.g., maternal infections) are non-specific risk factors for multiple symptoms—not limited to ASD or schizophrenia—but extending to spectrum phenotypes, including negative symptoms[1,2,36,44]. In the MIA model, adult offspring of infected mothers display a Purkinje-cell loss in lobule VII[53], reminiscent of human pathological findings[66]. Caution is required when interpreting animal behavior for comparing clinical outcomes since animal models do not fully replicate all the aspects of mental disorders. First, microglial blunting has been observed in patients with schizophrenia[32,*butseealso*74]. Second, stress after puberty retains microglial reactivity in different contexts[72,75]. Third, the reactive or neuroprotective microglia, including SAMs, warrant cerebellar vulnerability as the cell entity in the diathesis-stress model. Further, microglia replacement or modulation provides a therapeutic possibility for disorder phenotypes caused by aberrant inflammation[1,30,31,44,72,76]. Our results demonstrated the restoration of microglia accumulation, morphology, and reactivity by microglia replacement at least in the mouse model (Fig. 10), suggesting that disorder-associated microglia via accumulating stress leads to the synergistic impairments of cerebellar neuronal plasticity and brain-wide cognitive functions[38–40]. The limitation of our microglia replacement is that depletion was applied during the second stress protocol, preventing the changes, while we did not attempt to rescue established phenotypes. Although the experimental outcomes remain unknown, the recovery may depend on the timing of microglia depletion since microglial turnover (Fig. 2) and Purkinje cell death (Supplementary Fig. 18) continued for at least 4 weeks after RSDS. Another limitation is that cerebellum-specific depletion was tested only in male mice (Fig. 10). Since the estrous cycle begins four weeks after birth and microglia are influenced by this cycle and estrogen, the effects of systemic and cerebellum-specific microglia depletion and repopulation may vary among females based on their estrous cycle. Further discussion is given in Supplementary Discussion. These warrant further investigation.

Collectively, our study identified unique immune cells in the cerebellum that cause cerebellar vulnerability and influence cognition and behaviors. Brain activity along the cerebellum-associated pathways was attenuated in 2HIT sus mice. In stress models, microglial turnover and reactivity synergistically resulted in neurophysiological disruptions and neurodegeneration. SAMs were differentiated in the 2HIT model cerebellum via specific molecular patterns. These SAMs are considered a form of DAMs in the light of specific stress models.

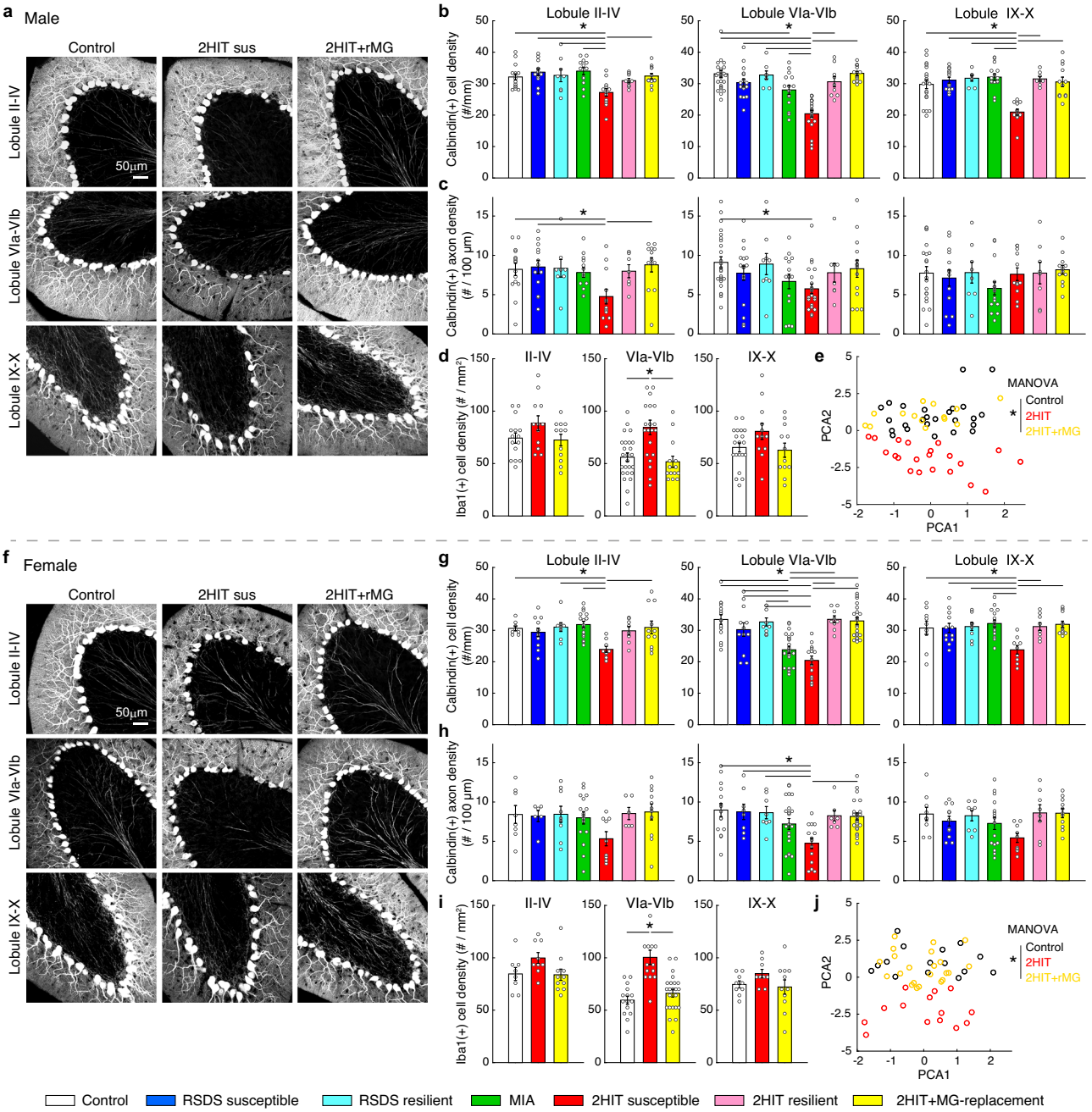

Fig. 6 | Microglia-dependent neural loss in the 2HIT cerebellar cortex. a Loss of Purkinje cells in the male cerebellar cortex. Representative images of cerebellar cortical lobules stained with anti-Calbindin antibody from Control, 2HIT-susceptible (2HIT sus), and 2HIT after microglia replacement (2HIT+rMG) groups are shown. Density graphs of Purkinje neurons (**b**) and axons (**c**) was significantly reduced, and that of microglia (**d**) was significantly increased, typically in the central lobule (VIa-VIb) of the 2HIT cerebellar cortex. Data in (**b**–**d**) are derived from identical slices. Data are shown as mean ± SEM. $^*p < 0.05$, one-way ANOVA with *multiple comparisons* using the Tukey-Kramer method. **e** Correlation analysis indicating a decrease in Purkinje cell and axon density and an increase in 2HIT sus microglia in males. Principal component analysis (PCA) distinguishes data distribution among Purkinje cell, axon, and microglia density from identical slices across Control, 2HIT sus, and 2HIT+rMG groups. $^*p < 1.6 \times 10^{-11}$, MANOVA. **f** Loss of Purkinje cells in the female cerebellar cortex. Representative images of cerebellar cortical lobules of Control, 2HIT sus, and 2HIT+rMG are shown. Density graphs of Purkinje neurons (**g**) and axons (**h**) was significantly reduced, and that of microglia (**i**) was significantly increased ($^*p < 0.05$), typically in lobule VIa-VIb of the cerebellar cortex. **j** Correlation analysis indicating a decrease in Purkinje cell and axon density and an increase in 2HIT sus microglia in females. PCA separates the data distribution among three datasets. $^*p < 6.0 \times 10^{-10}$, MANOVA.

Degeneration of cerebellar Purkinje cells and reduced excitability of remaining neurons may lead to deficiencies in self- and external recognition via cognitive-behavioral anomalies. Targeting aberrant cerebellar microglia/macrophages mitigated cellular disruptions, offering a promising avenue for drug discovery in complex inflammatory stress-associated disorders.

Methods

Mice

C57BL/6N, BALB/c, and ICR mice were purchased from Japan SLC and CLEA Japan. Three to five mice from the same experimental group were housed in each cage with free access to food (Pellet chow: PMI Nutrition International, USA, or Oriental Yeast Co., Ltd, Japan)

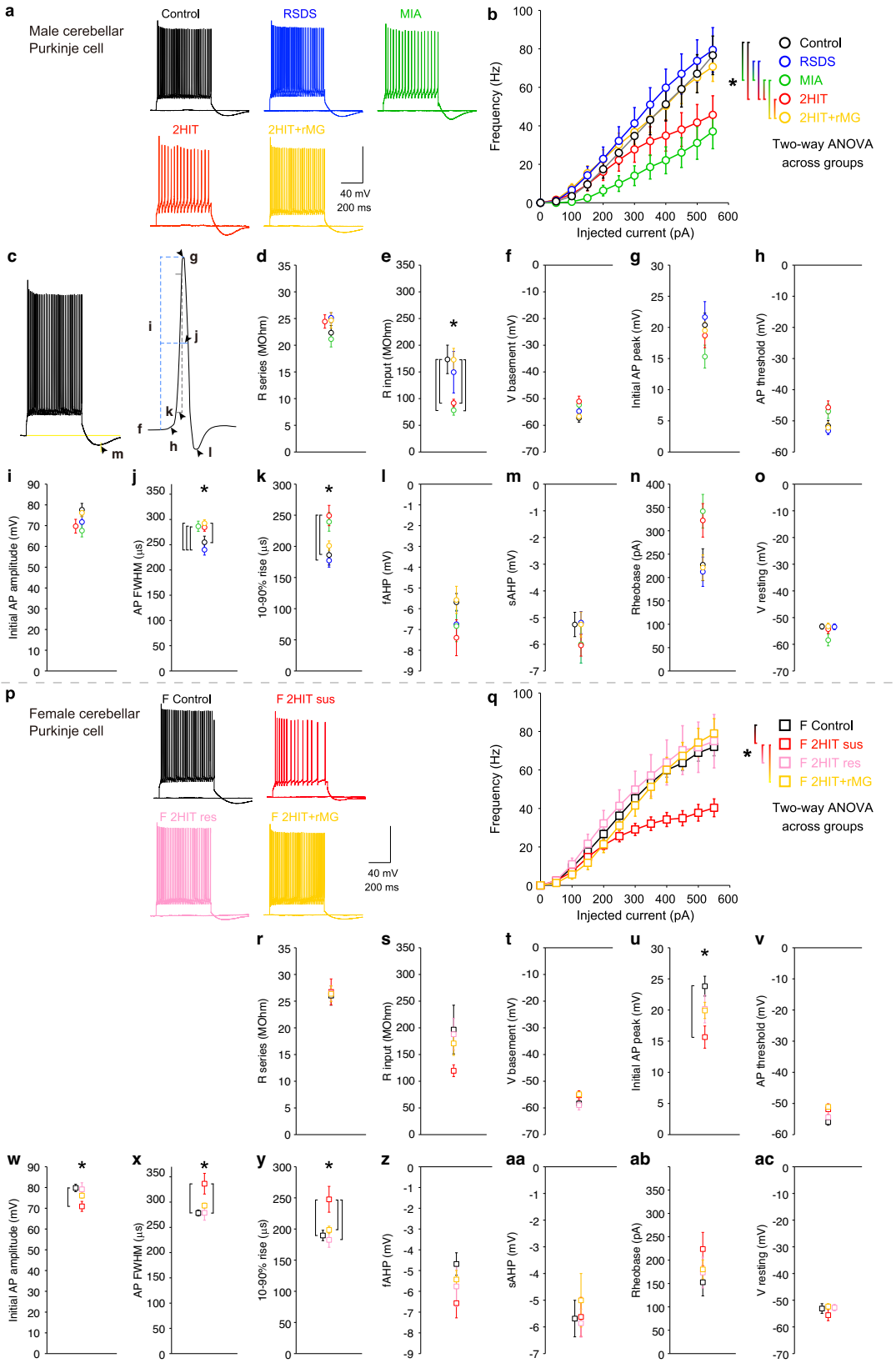

and water in a specific pathogen-free, temperature- and humidity-controlled room (22 ± 3 °C, 50 ± 10% RH) under a 12-h light period, 12-h dark period (lights on from 8:00–20:00) cycle. All procedures for animal care and use were following the National Institutes of Health Guide for the Care and Use of Laboratory Animals and were approved by the Animal Care and Use Committees of Kyoto University Graduate School of Medicine. All animal handling and reporting comply with ARRIVE guidelines. In this study, unless otherwise stated, a control experiment refers to a group of mice that did not receive any conditioning (Control), while a control

Fig. 7 | Low excitability of cerebellar Purkinje neurons of 2HIT-susceptible mice. **a** Representative action potentials of male cerebellar Purkinje cells, evoked by 400 pA and 500 ms step-pulse current injection. **b** Firing frequency of male mice of Control, RSDS-susceptible (RSDS), MIA, 2HIT-susceptible (2HIT), and 2HIT after microglia replacement (2HIT+rMG) Purkinje cells in response to gradually increased depolarization pulses from 0 to 550 pA. Two-way ANOVA group × injected current, interaction: $F(40, 1364) = 1.00$, $p = 0.4765$; main effect of group: $F(4, 1364) = 24.3$, $p < 0.0001$. $^*p < 0.05$, *multiple comparisons* using the Bonferroni method. **c** Drawings of action potential waveform (left, a representative response to 400 pA pulse; right, single action potential and parameters (**f**-**m**). **d**-**o** Purkinje cell action potential properties, including series resistance (**d**), input resistance (**e**), basement potential of action potential (**f**), peak voltage of action potential (**g**), action potential threshold (**h**), amplitude of action potential (**i**), full width of half maximum (FWHM) (**j**), 10–90% rise time (**k**), fast afterhyperpolarization of the single action potential (fAHP) (**l**), slow afterhyperpolarization following action potential burst (sAHP) by 400 pA pulse (**m**), rheobase (**n**), and resting potential (**o**) are shown. All action potentials were measured in the initial action potential when evoked by the minimum depolarization pulses with a 50-pA step. The input resistance was measured as the current during 80 ms and 5 mV hyperpolarization pulse. The resting potential was measured as the voltage without current injection. $^*p < 0.05$, one-way ANOVA with *multiple comparisons* using the Tukey-Kramer method. **p** Representative action potentials of female cerebellar Purkinje cells. **q** Firing frequency of female mice of Control, 2HIT-susceptible (2HIT sus), 2HIT-resilient (2HIT res), and 2HIT+rMG Purkinje cells in response to gradually increased depolarization pulses from 0 to 550 pA. Two-way ANOVA group × injected current, interaction: $F(30, 990) = 1.08$, $p = 0.3526$; main effect of group: $F(3, 990) = 15.47$, $p < 0.0001$. $^*p < 0.001$, *multiple comparisons* using the Bonferroni method. **r**-**ac** Purkinje cell action potential properties are shown. $^*p < 0.05$, one-way ANOVA with *multiple comparisons* using the Tukey-Kramer method. All data are represented as mean ± SEM.

experiment with 2HIT mice corresponds to each conditioning and the Control group.

Human

FFPE-fixed human brain samples from each patient with ALS and control were obtained at Nagoya University Hospital via Japan Brain Bank Net. All procedures for human postmortem subject use were in accordance with the Declaration of Helsinki, and the study protocol was approved by the Ethics Committee of the Aichi Medical University and the Ethics Committee of Kyoto University Graduate School of Medicine (R4048). Written informed consent was obtained from all patients.

Maternal immune activation

Maternal immune activation (MIA) was applied according to previous studies[31,77] with minor modifications. Virgin female mice (10–14 weeks of age) were plug-checked in the morning after mating in the previous day's evening. The appearance of a vaginal plug was discerned as embryonic day 0.5 (E0.5). Pregnant C57BL/6N dams received injection once intraperitoneally with 10 mg/kg poly(I:C) (tlrl-pic, InvivoGen, San Diego, USA) at E12.5. For the MIA control, we injected endotoxin-free sterile water (Supplementary Fig. 1b), but we did not use MIA control in other experiments. Different poly(I:C) products can induce varying immune responses and can differentially affect maternal physiology and pregnancy outcomes[11]. We confirmed the inflammatory responses after poly(I:C) injection by monitoring hypothermia, lasting for 4.5 h, in injected females[11]. We only investigated the batch delivered from dams that showed a temperature drop after the injection (~2.5 °C at 4 h after injection) (Supplementary Fig. 1b). Offspring were weaned at postnatal day 21 (PND21) and were caged randomly to avoid confronting litter. We applied as same MIA protocol to pregnant BALB/c dams to validate the strain difference in the 2HIT model (Supplementary Fig. 5). In this study, animals from different parents were mixed for experiments; the pups were gathered in the same experimental group.

Social defeat stress

Repeated social defeat stress (RSDS) was applied to male mice according to the previous study[78]. Briefly, male ICR mice were screened for aggressiveness toward male C57BL/6N mice, measured by attack latency and attack frequency during an observation period (180 s). Eligible mice were used as aggressors for RSDS. On the day of RSDS start (either at 4 or 9 weeks of age), each isolated mouse to be defeated was introduced into the home cage of a resident male aggressor ICR mouse for 10 min daily for ten consecutive days. Pairs of defeated and aggressor mice were randomized daily to minimize bias in the aggressiveness of aggressor ICR mice. SDS was applied in the sound-attenuated room under dim light. For the RSDS control experiment, Control mice were placed in a novel cage for 10 min daily over the same period. Each mouse was subjected to a social avoidance test with or without prior RSDS. RSDS controls showed no significant differences (Δinteraction zone time −9.4 ± 7.1 s, Δavoidance zone time 17.4 ± 12.2 s, $n = 13$, $p = 0.7423$, Wilcoxon rank sum test). We assessed basic locomotor activity after RSDS and found no severe motor deficits; however, we confirmed motor deficits and motor dyscoordination four weeks later (Fig. 9k-m). We applied the same protocol to BALB/c male mice. To establish the female 2HIT model, we applied RSDS to female mice according to a previous study[79] with minor modifications. Briefly, male odorants were applied to the female mice to induce attacks from the male aggressor ICR. We collected male ICR urine using metabolic cages, stored at 4 °C, and used within 2–3 days after collection. Urine suppliers, female mice, and aggressor mice were randomized daily. Urine was applied at the base of the tail (20 µl) and on the vaginal orifice (20 µl) just before RSDS and immediately placed in the home cage of a resident male aggressor ICR mouse for 10 min same as male RSDS. Throughout the RSDS session, we counted the number of the chased (5–30 s relentless tracking) and attacks (fierce attacks stirring up the cage bedding) (Supplementary Fig. 1p, q). No mounting behaviors and pregnancies were observed.

Social avoidance test

Social avoidance tests were conducted at five weeks of age, from the day after the RSDS condition. A mouse was kept for 180 s in an open field chamber (30 W × 40 D × 20 H cm^3) with a wire mesh cage (10 W × 6D × 30 H cm^3) enclosing an unfamiliar ICR mouse as the aggressor located at one end of the field. The trajectory of the subject mouse was monitored and automatically measured by ANY-maze Behavioral tracking software (Muromachi Kikai Co., Ltd, Japan). A 30 W × 14 D cm^2 rectangular zone, including the wire mesh cage, was defined as the social interaction zone. A 30 W × 8 D cm^2 rectangular zone opposite the social interaction zone was defined as the social avoidance zone. The duration that each mouse spent in the respective zones was used as indices for the levels of social interaction and social avoidance. One day before the social avoidance test, mice were habituated to the test chamber without an ICR mouse. In this study, we defined susceptible mice as those that showed social interaction for ICR (+) - ICR (-) < −40 s and social avoidance for ICR (+) - ICR (-) > 40 s during the observation period. Resilient mice were defined as those that showed social interaction for ICR (+) - ICR (-) > −40 s and social avoidance for ICR (+) - ICR (-) < 40 s during the observation period (Supplementary Fig. 1f-o). These criteria excluded mice that spent most of the time in the middle zone and were thus difficult to categorize as either susceptible or resilient. The proportion of susceptible and resilient in male and female RSDS and 2HIT are shown in Fig. 1b, respectively. We used both susceptible and resilient mice in this study. For male 2HIT, we often used only susceptible mice due to the rarity of male resilient. Since more than half of the female 2HIT were resilient, we used both susceptible and resilient in all experiments (Figs. 1, 3, 5, 6, 7, and 9).

Animal behavior tests

Behavior tests were performed in the daytime (11:00–16:00). Before that, the subject mice were acclimated in the experimental room for 1 h. Animal behaviors were tested from 9-week-old (RSDS at 4-week-old) or 11-week-old (RSDS at 9-week-old); the behaviors of mice exposed to RSDS at 4 weeks

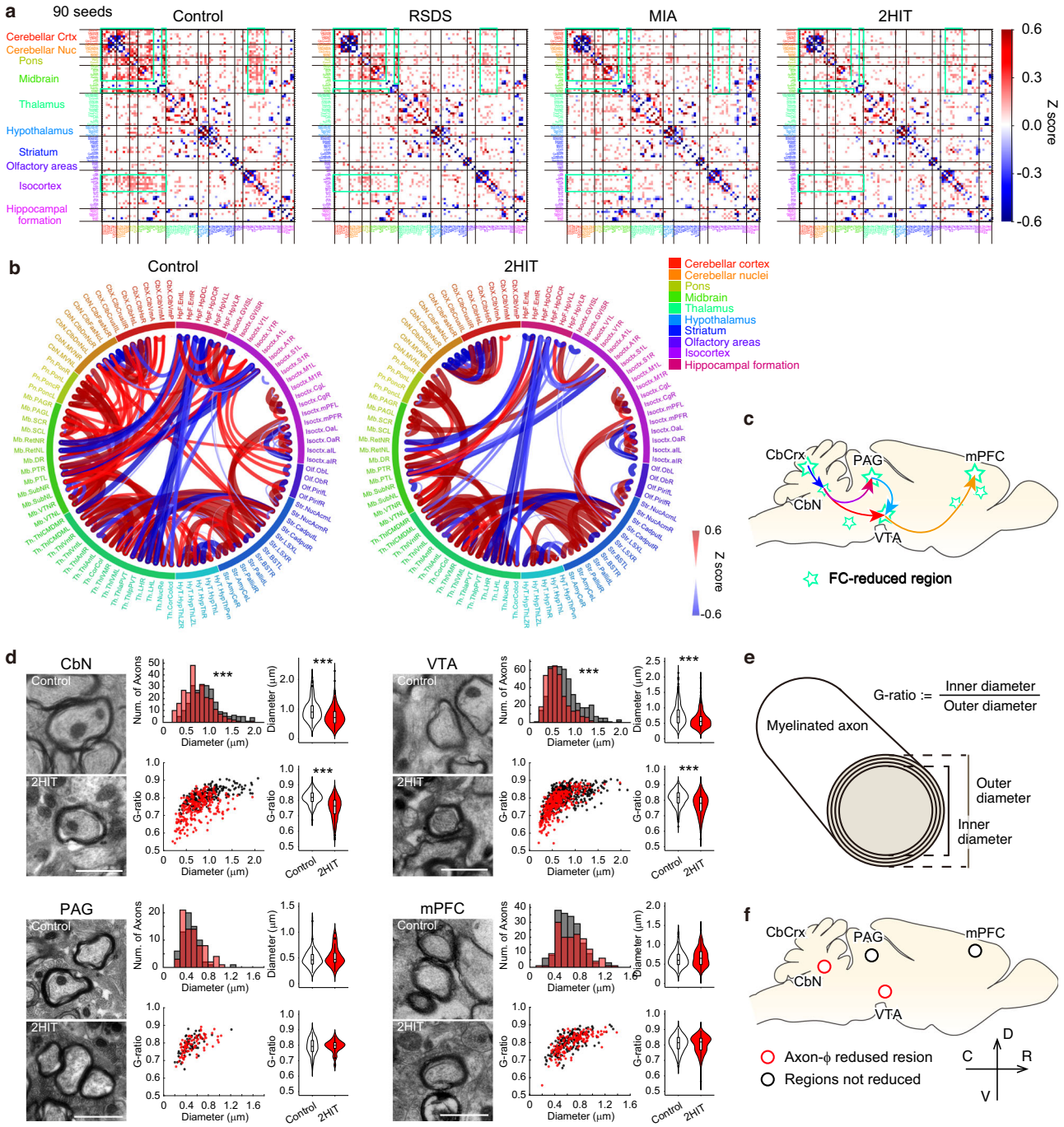

Fig. 8 | Disruption of the cerebellum-midbrain-prefrontal cortical functional connectivity and axon thinning in the cerebellar pathway. a Functional connectivity (FC) maps of stress-exposed male mice. Resting-state functional magnetic resonance imaging (rs-*f*MRI) was performed. 90 seeds were applied to entire brain. Seed-to-seed correlation maps are displayed as Z scores of correlation coefficients. Note the correlation declined in RSDS, MIA, and 2HIT, particularly between cerebellar cortex (including the cerebellar vermis and hemispheres), cerebellar nuclei (dentate and fastigial nuclei), dorsal and ventral midbrain (PAG and VTA), and prefrontal cortex (mPFC, cingulate cortex [Cg], and primary motor cortex [M1]), highlighted with turquoise rectangles. **b** Inter-regional correlations of brain-wide blood oxygenation level-dependent (BOLD) signals (Control vs. 2HIT). **c** Regions with decreased FC in the 2HIT mouse brain. **d** Electron microscopy analysis of axons. Axon diameters and g-ratios were measured in various brain regions of male Control and 2HIT mice. Representative axon images (*left*, scale bar = 1 μm), histograms of axon diameters, g-ratio vs. axon diameter plots (*middle*), and violin plots with whiskered boxplots (*right*) are shown. $^{***}p < 0.001$, two-sample Kolmogorov-Smirnov test (histogram) and Wilcoxon rank sum test applied Bonferroni correction (violin plot). **e** Definition of g-ratio. The g-ratio is the ratio of the inner diameter of an axon to its outer diameter, including the myelin sheath. **f** Axon diameter reductions observed in CbN and VTA in the 2HIT models.

are shown in Fig. 9 (males and females) and in Fig. 10 (males) and at 9 weeks in Supplementary Fig. 23 (males). Before undergoing behavioral tests, female mice were subjected to vaginal lavage to confirm estrous cycle stages. The vaginal smears were flushed with 20 μl PBS, inserting the tip carefully into the vagina. The fluid was placed on a glass slide to dry, then gently washed and observed under a stereo microscope. To exclude the impacts of the estrous cycle, behavior tests on the female mice in the estrus stage were performed on different days.

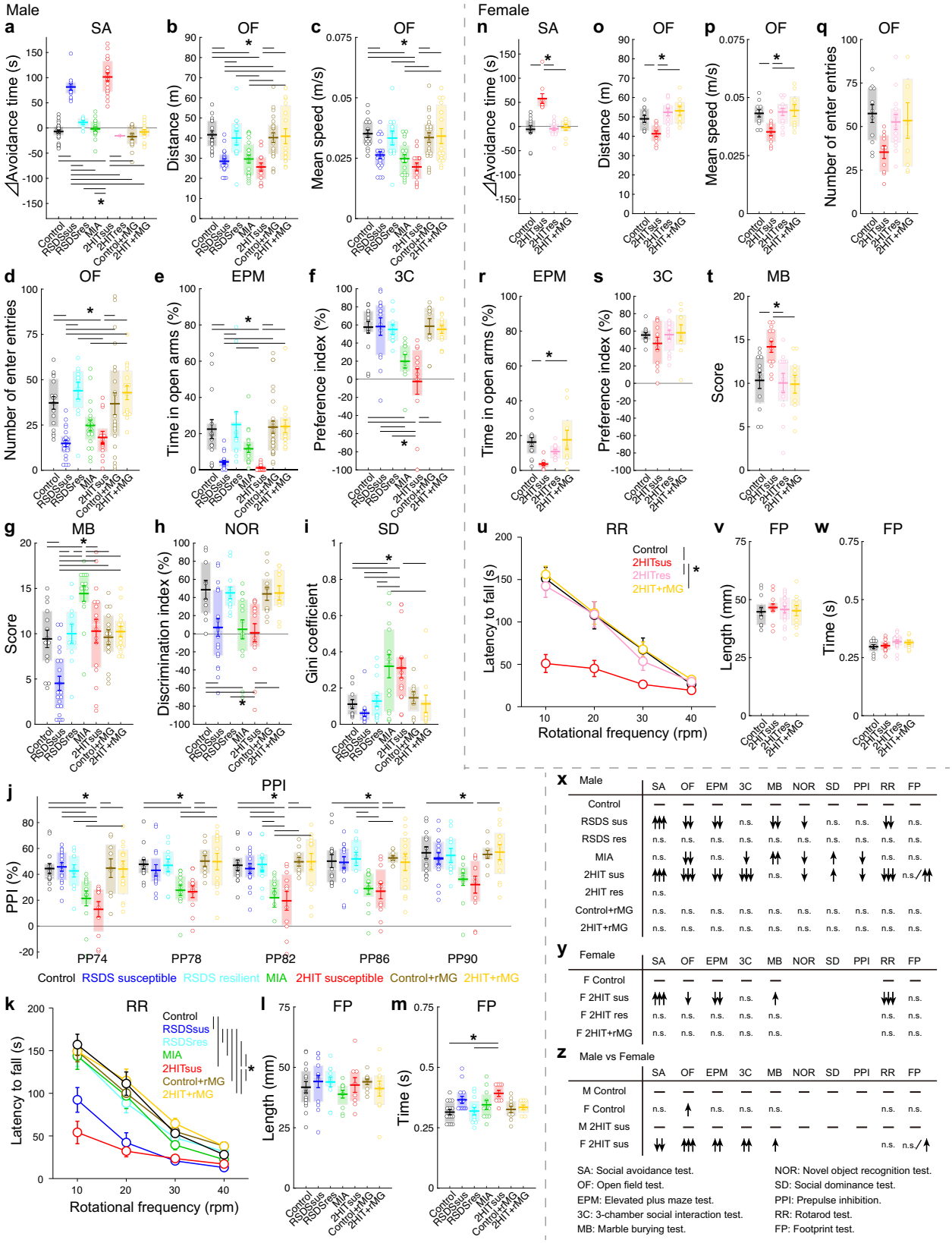

Open field test

After the habituation, a mouse was individually placed in the center of the Plexiglas open-field arena (40 × 40 cm^2, 30-cm high white walls and floor). We monitored the behavior of the freely moving mouse for 20 min using a video camera. The center zone was defined as the 16 × 16 cm^2 square in the center of the arena. The traveling distance, mean speed, and the number of entries into the center zone were compared among the groups. The arena and surrounding walls were cleaned and deodorized with H_2O and 70% EtOH before each session. Exploration behavior was quantified using ANY-maze

Fig. 9 | Exacerbation of animal behaviors and motor coordination deficits due to cumulative stress, and its amelioration with microglia replacement. **a**-**m** and **x** represent outcomes of male animals; **n**–**w** and **y** represent female animals. **a** Social avoidance time. Differences in time spent in the avoidance zone with versus without a stressor mouse are shown for male Control, RSDS susceptible (sus), RSDS resilient (res), MIA, 2HIT sus, Control after microglia replacement (Control+rMG), and 2HIT+rMG. Data for male 2HIT resilient animals ($n = 1$) is included from the same experimental subset, while omitted due to rarity in following experiments. Open field test: Total distance traveled (**b**), average speed (**c**), and number of center entries (**d**). **e** Time spent in open arms of the elevated plus maze. **f** Preference index of 3-chamber test. **g** Marble burying score. **h** Discrimination index of novel object recognition test. **i** Social dominance test. **j** Prepulse inhibition (PPI) measured at five prepulse intensities (74, 78, 82, 86, and 90 dB). **k** Motor coordination on the rotarod. Latencies to fall from the rod rotating at 10, 20, 30, and 40 rpm are shown. Two-way ANOVA group × rotation frequency, interaction: $F(18, 328) = 2.3599$, $p < 0.0001$. Stride length (**l**) and stride time (**m**) of hind paws in footprint analysis. No apparent ataxia was noted in the footprint test, although stride time was extended in the 2HIT group. **n** Social avoidance time for female Control, 2HIT sus, 2HIT res, and 2HIT +rMG groups. **o**-**q** Open field test. **r** Elevated plus maze test. **s** 3-chamber test. **t** Marble burying score. **u** Motor coordination on the rotarod. Two-way ANOVA group × rotation frequency, interaction: $F(9, 176) = 2.9769$, $p < 0.0001$. Stride length (**v**) and stride time (**w**) in footprint analysis. Data represent mean ± SEM overlaid with box plot. *$p < 0.05$, one-way ANOVA (**a**-**j**, **l**, **m**, **n**–**t**, **v**, and **w**) with *multiple comparisons* using the Tukey-Kramer method. *$p < 0.0001$, two-way ANOVA (**k** and **u**) with *multiple comparisons* using the Bonferroni method. Summary table of male (**x**) and female (**y**) behavior outcomes. The number of arrows represents different significant levels compared to Control (↓/↑, $p < 0.05$; ↓↓/↑↑, $p < 0.01$; and ↓↓↓/↑↑↑, $p < 0.001$). **z** Summary table of comparison between male and female behavior outcomes. The number of arrows represents different significant levels for females compared to males as the standard (↓/↑, $p < 0.05$; ↓↓/↑↑, $p < 0.01$; and ↓↓↓/↑↑↑, $p < 0.001$, Wilcoxon rank sum test).

Behavioural tracking software (Muromachi Kikai Co., Ltd) (Fig. 9b-d, Fig. 10r-t: male, Fig. 9o-q, female, and Supplementary Fig. 23d, male RSDS at 9 weeks).

Elevated plus maze test

An elevated plus maze is composed of two open arms (5 cm wide, 25 cm long, without walls) and two closed arms (5 cm wide, 25 cm long, with 15 cm walls) interconnected by a central area of 5 cm square. The cross maze is located at a height of 50 cm from the floor. After acclimation to a test environment, a mouse was transferred to the center of the elevated plus maze and kept in the maze for 5 min. Mouse behaviors were video-monitored, and the exploration time was manually measured using a stopwatch in a single-blind test or was analyzed with Smart 3.0 software (Panlab Harvard Apparatus) and MATLAB. We obtained the proportion of the time that the mouse spent in the open arms during the observation period (Fig. 9e, Fig. 10u, male; Fig. 9r, female; and Supplementary Fig. 23e, male RSDS at 9 weeks).

3-chamber social interaction test

The sociability of a mouse was tested in a Plexiglas three-chambered open-field arena (60×40 cm^2, 30 cm high) with small circular wire cages (10 cm in diameter, 16 cm high) in two corners. First, a mouse was allowed to explore the arena for 10 min to determine the baseline of exploratory behavior against the novel subjects without a social target. Next, a stranger mouse was placed into one cage, and the movement was monitored for another 10 min. Mouse behaviors were video monitored and were analyzed with Smart 3.0 software and MATLAB. We compared time spent in the interaction and overall locomotion by an examiner in a blinded experimental condition. The preference index (PI) of the 3-chamber social interaction test was calculated as follows: = (Time A − Time B)/(Time A + Time B)*100, where interaction with a mouse is A and interaction with an empty cage is B (Fig. 9f, Fig. 10v, male; Fig. 9s, female; and Supplementary Fig. 23f, male RSDS at 9 weeks).

Marble burying test

The marble burying is a test for stereotyped repetitive behaviors in rodents analogous to those observed in autistic phenotypes. Tests were conducted in a testing cage (25×15 cm^2, 12-cm high). Bedding tips as wood shavings were covered to a depth of 3 cm. Twenty glass marbles (17 mm in diameter) were aligned equidistantly in four rows of five marbles each. Spaces (3–4 cm width) were made for placing animals. At the end of the 10-minute test period, a mouse was removed from the cages. The marble burying score was defined following the criteria: 1 for marbles covered > 50% with bedding, 0.5 for marbles covered ~50% with bedding, and 0 for marbles less covered (Fig. 9g, Fig. 10w, male; Fig. 9t, female; and Supplementary Fig. 23g, male RSDS at 9 weeks).

Novel object recognition test

The novel object recognition test comprised three parts performed on four days. The first part was habituation. On days 1-3, mice were put into a non-transparent box ($30 \times 40 \times 20$ cm^3) for 10 min to allow habituation to the manipulations and environment. On day 4, mice were put into the same box with two identical objects (5 cm in diameter, 8 cm high, transparent object) for 10 min to explore and recognize the objects. After 30 min, mice were individually put into the box with one novel object (5 cm in diameter, 8 cm high, black object) for 5 min. The movements of mice in the box were monitored with a video camera and analyzed with Smart 3.0 software. The discrimination index of the 3-chamber social interaction test was calculated as follows: = (Time near A – Time near B)/(Time near A + Time near B)*100, where a novel object is A and a non-novel object is B (Fig. 9h, male RSDS at 4 weeks; and Supplementary Fig. 23h, male RSDS at 9 weeks).

Social dominance test

A rectangular plastic cage (32×25 cm^2) was set on ice. And the floor was cooled down to 5 ± 3°C. A small heating pad was placed underneath the narrow corner of the cage (6×8.5 cm^2) to warm the local temperature to 35 °C. The temperature was measured using an infrared thermometer. Four subjected mice from different cages were mixed randomly. Animals were placed in a cold cage without a warm spot for 30 min and let them cool down, and then the mice were transferred to the test cage where the animals competed for the warm spot. The behaviors of the four mice in the test cage were video-monitored for 20 min, and the occupation time for the warm spot of each mouse was acquired with Smart 3.0 software. The Gini coefficient: (=1–2*(Σo.t.(n)), where o.t. (n) means the occupation time of each mouse) was calculated from the occupation time for the warm spot across animals. When Gini coefficient is high, the statistical dispersion is high, and occupation time is inequal among four animals. A few strong mice tend to occupy the warm place longer and others are excluded during experiment time (Fig. 9i, male RSDS at 4 weeks; and Supplementary Fig. 23i, male RSDS at 9 weeks).

Prepulse inhibition

The startle response and prepulse inhibition (PPI) were measured using a startle reflex measurement system (San Diego Instruments, Inc., USA). The test session began by placing a male mouse in a plastic cylinder and leaving it undisturbed for 30 min. The background white noise level in the chamber was 70 decibels (dB). A prepulse trial started with a 50-ms null period, followed by a 20-ms prepulse white noise (74, 78, 82, 86, and 90 dB). After a 100-ms delay, the startle stimulus (a 40-ms, 120 dB white noise) was presented, followed by a 290-ms recording time. The total duration of each trial was 500 ms. A test session consisted of six trial types (pulse-only trial, and five types of prepulse-pulse trial). Six blocks of the six trial types were presented in a pseudorandomized order such that each trial type was

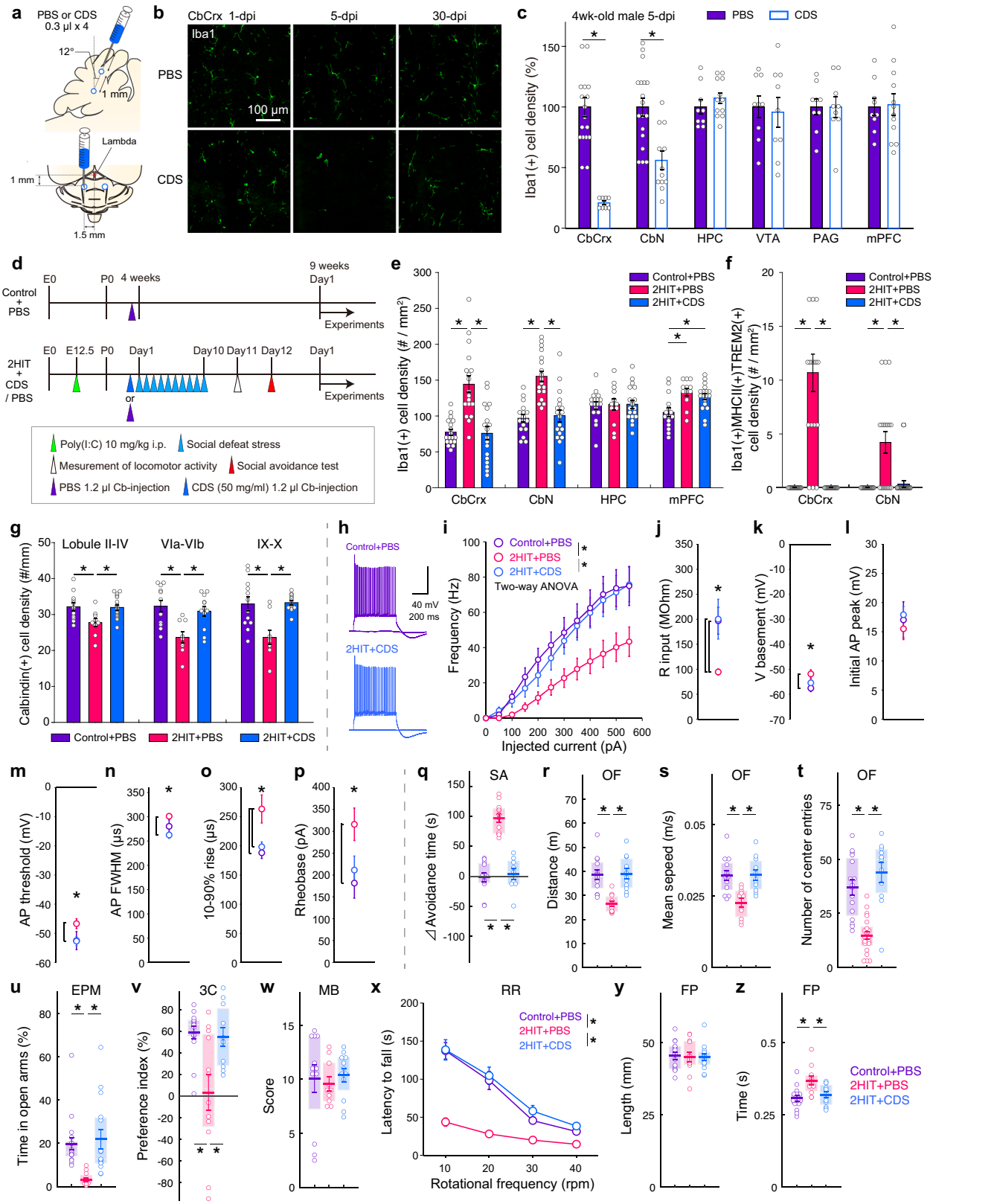

presented once within a block. The formula: =100*(1-response on acoustic prepulse stimulus trials/startle response on pulse-only trials), was used to calculate %PPI (Fig. 9j, male RSDS at 4 weeks; and Supplementary Fig. 23j, male RSDS at 9 weeks).

Rotarod test

Performance on the rotarod was evaluated using Rotarod370 (Bio-medica, Japan) with a rod (4 cm diameter, 4 lanes) that was set to rotate at each frequency (10, 20, 30, and 40 rpm). To ensure that mice could stay stably on

Fig. 10 | Amelioration of 2HIT phenotypes with cerebellum-specific microglia replacement. a Schematic of stereotaxic injection of PBS or clodronate disodium salt (CDS) into the male cerebellum. PBS or CDS was administered at four sites in 4-week-old male mice. **b** Representative images of Iba1(+) microglia in the cerebellar cortex at 1-, 5-, and 30-days post-injection (dpi) of PBS or CDS. **c** Percent changes in Iba1(+) microglia count across brain regions at 5 dpi of PBS or CDS. Bar graphs show data from the cerebellar cortex (CbCrx), cerebellar nuclei (CbN), hippocampus (HPC), ventral tegmental areas (VTA), periaqueductal gray (PAG), and medial prefrontal cortex (mPFC). $^*p < 0.05$, two-tailed unpaired Student's *t*-test. **d** Experimental timeline for Control+PBS, 2HIT + PBS, and 2HIT + CDS groups. **e** Iba1(+) microglia cell density in 9-week-old Control+PBS, 2HIT + PBS, and 2HIT + CDS animals (five weeks post-injection of PBS or CDS); see also Fig. 1d. **f** Density of Iba1-, MHC class II-, TREM2-triple-positive cells from CbCrx and CbN for Control+PBS, 2HIT + PBS, and 2HIT + CDS; see also Fig. 5i. **g** Bar graphs showing the density of cerebellar Purkinje cells in Control+PBS, 2HIT + PBS, and 2HIT + CDS groups. Data from lobules II-IV, VIa- VIb, and IX-X are presented (mean ± SEM). $^*p < 0.05$, one-way ANOVA with *multiple comparisons* using the Tukey-Kramer method (**e**–**g**). **h** Representative action potential traces of Purkinje cells from Control+PBS and 2HIT + CDS mice evoked by 400 pA and 500 ms step-pulse current. **i** Firing frequency of Purkinje cells from Control+PBS, 2HIT + PBS, and 2HIT + CDS groups in response to gradually increasing depolarization pulses from 0 to 550 pA. Two-way ANOVA group × injected current, interaction: $F(20, 770) = 0.78$, $p = 0.7412$; main effect of group: $F(2, 770) = 37.64$, $p < 0.0001$. $^*p < 0.001$, *multiple comparisons* using the Bonferroni method. Purkinje cell action potential properties, including input resistance (**j**), basement potential of action potential (**k**), peak voltage of action potential (**l**), action potential threshold (**m**), full width of half maximum (FWHM) (**n**), 10–90% rise time (**o**), and rheobase (**p**) is shown. There are significant differences between Control+PBS and 2HIT + PBS or between 2HIT + PBS and 2HIT + CDS in (**j**), (**k**), (**m**), (**n**), (**o**), and (**p**). **q**-**z** Behavioral tests in Control+PBS, 2HIT + PBS, and 2HIT + CDS mice: social avoidance time in response to a stressor in the social avoidance test (**q**); open field test measures of travel distance (**r**), mean speed (**s**), and center entries (**t**); time spent in open arms of the elevated plus maze (**u**); preference index in the 3-chamber test (**v**); marble burying score (**w**); motor coordination assessed by latency to fall on a rotating rod at 10, 20, 30, and 40 rpm (**x**) [Two-way ANOVA group × rotation frequency, interaction: $F(6, 148) = 6.2535$, $p < 0.0001$]; and hind paw stride length (**y**) and stride time (**z**) in footprint analysis. $^*p < 0.05$, one-way ANOVA with *multiple comparisons* using the Tukey-Kramer method (**q**-**w**,**y**,**z**). $^*p < 0.001$, two-way ANOVA with *multiple comparisons* using the Bonferroni method (**x**). All data are represented as mean ± SEM.

the rod, mice were placed on the resting rod for at least 30 s before the experiment. The rotational frequency accelerated from 0 rpm to each frequency over 15 s and then held constant for 5 min. The latency to fall was recorded automatically by photosensors. The apparatus was cleaned with 70% EtOH and air-dried before each session (Fig. 9k, Fig. 10x, male; and Fig. 9u, female).

Footprint analysis

Animals were placed at the end of a one-directional passageway (3 cm in width and 30 cm in length) with a transparent floor at a height of 13 cm, and they were allowed to walk straight forward while being recorded with a micro video camera from below. Each animal was tested more than three times for walking. Extracted still images from the video were analyzed manually for the distance of the center position of the hind paws and the duration time in a single-blind test, and three data for each trial were collected and averaged (Fig. 9l, m, Fig. 10y, z, male; and Fig. 9v, w, female).

CSF1R inhibitor treatment

Colony-stimulating-factor 1 receptor (CSF1R) inhibitor treatment was performed according to the previous study[44]. For pharmacological microglia depletion, the CSF1R inhibitor Ki20227 (Biorbyt Ltd., UK) was given to 4-week-old C57BL/6N mice by oral administration of 0.2 mL/day (20 mg/mL dissolved to 10% DMSO and 90% corn oil) for seven days (Fig. 1a and Supplementary Fig. 1r, s). Ki20227 (IC50 = 2 nM to M-CSF receptor; 451 nM to c-Kit)[80].

We performed behavioral experiments to assess the effect of Ki20227 on wild-type C57BL/6 male mice. Behavioral experiments included tests for social avoidance, open field, elevated plus maze, three-chamber, marble burying, novel object recognition, social dominance, PPI, and motor coordination (rotarod, footprint tests) tests did not show any anomalies (Fig. 9, Control+microglia replacement), indicating no significant difference in behavioral anomalies related to depressiveness, anxiety, neurodevelopmental disorder-like, and schizophrenia-like behaviors. Other disorder-like behaviors, such as eating and sleep disorders, remain unknown. And both Ki20227-treated mice of Control and 2HIT mice (Control+microglia replacement and 2HIT+microglia replacement) remained healthy, with no deaths observed in our breeding environment after injection.

Cerebellum-specific microglia depletion

We applied clodronate disodium salt (CDS; Tokyo Chemical Industry, Japan) to deplete microglia in the cerebellum[72]. After stereotaxic surgery was performed, we started surgery after the animals' breath and pulse were stabilized and the extent of anesthesia was enough, without corneal reflection, touch, and pinch responses under anesthesia with 1–3% isoflurane (VTRS, Viatris, US) in oxygen[44,72]. A mouse was fixed to the stereotaxic apparatus (Model 900 Small Animal Stereotaxic Instrument, KOPF INSTRUMENTS, US), analgesics (Xylocaine Jelly, SandozAG, Switzerland) were applied, and a longitudinal skin incision was made to expose the skull. Two small holes (300 µm radius) were drilled in the skull (1.5 mm left and right sides from the median line 1 mm posterior to lambda), following which a micro syringe was inserted at the depths of 1 mm and 2 mm on both sides (12° from vertical). We injected 0.3 µL of PBS or CDS (50 mg/ml in PBS) at four sites (shallow/deep and left/right) for a total of 1.2 µL into the cerebellum of 4-week-old C57BL/6 N mice (Fig. 10a). After injection of either PBS or CDS, the needle was kept in place for 5 min to avoid reflux of the substances before retracting it. Following the surgery, the animals were placed back in their home cage and closely monitored. This total 1.2 µL injection of 50 mg/ml CDS did not cause postoperative seizures. Microglia depletion by CDS is maximal 5 days post injection and refilled 10–20 days later[72]. We administered CDS one day before RSDS ($n = 15$) and in addition on day 7 of RSDS ($n = 2$), observing no differences in animal behavior. We combined both datasets as 2HIT + CDS.

Immunohistochemistry

Immunohistochemistry was performed according to the previous study[44]. Mice aged 2, 5, and 9 weeks (both male and female) were used for the immunohistochemistry. After briefly applying anesthesia with 0.9% ketamine (Daiichi Sankyo Co., Ltd.) and 0.2% xylazine (Bayer AG) (i.p., 150 µL), the brains were extracted, perfused, and fixed with 4% paraformaldehyde (PFA). The brains were kept in PFA for 2 days at 4 °C. After submersion in PBS containing 30% sucrose for 4–7 days for dehydration, 50-µm cryosections were collected in water. Sections were heated in HistoVT (Nacalai Tesque, Japan) to 80 °C for 30 min, rinsed in tris buffered saline (TBS), and incubated in blocking solution (TBS containing Blocking One (Nacalai Tesque) and 0.5% Triton) for 1 h at 20–24 °C. Sections were then incubated with primary antibody at 4 °C for 48 h. For single-staining of microglia, we used rabbit anti-Iba1 (1:1000 dilution [0.5–0.7 µg/mL], 019-19741; FUJIFILM Wako Pure Chemical) as the primary antibody. Then, the sections were washed for 5 min three times at room temperature in TBS and were incubated with Alexa Fluor 647-labeled secondary antibodies (1:200-250 dilution [8-10 µg/mL], ab150079; Abcam) for 2 h at room temperature. Subsequently, sections were rinsed three times in TBS for 5 min each and were mounted on glass slides and coverslipped with VECTASHIELD Mounting Medium with DAPI (H-1200, Vector Lab, Inc, USA). For double-staining (Figs. 2 and 6), we used fluorescently conjugated-primary antibodies against Iba1 (Anti Iba1, Rabbit, Red Fluorochrome(635)-conjugated,

1:300; FUJIFILM Wako, 013-26471) together with Ki67 (Alexa Fluor® 488 Anti-Ki67 antibody [SP6], 1:100 [5 μg/mL]; Abcam, ab281847), Cleaved Caspase-3 (Alexa Fluor® 488 Cleaved Caspase-3 (Asp175) Antibody, 1:250; Cell Signaling #9669), or Calbindin (Alexa Fluor® 488 Anti-Calbindin antibody [EP3478], 1:200 [2.5 μg/mL]; Abcam, ab208377). Iba1 is a pan-microglia marker. Calbindin is a Purkinje-cell-specific marker in the cerebellum and is expressed in inhibitory interneurons in the mPFC (Supplementary Fig. 19). For triple-staining (Fig. 5g-l), we used fluorescently conjugated-primary antibodies against Iba1 (Anti Iba1, Rabbit, Red Fluorochrome(635)-conjugated, 1:300; FUJIFILM Wako, 013-26471) and two kinds of primary antibodies; rat anti-MHC class II (1:100-500 dilution [1-5 μg/mL]; Invitrogen, 14-5321-82) and goat anti-TREM2(1:100-500 dilution [1-5 μg/mL]; Abcam, ab95470). Secondary antibodies were anti-rat IgG Alexa Fluor 555 (1:250 dilution [8 μg/mL], ab175476; Abcam) and anti-goat IgG Alexa Fluor 488 (1: 250 dilution [8 μg/mL], ab150129; Abcam). Fluorescence images were obtained using an Olympus FV3000 confocal laser-scanning microscope equipped with UPLSAPO 30XS/1.05 NA or UPLXAPO 60XO/1.42NA oil immersion lens. The emission wavelength for imaging was 405, 488, and 640 nm, and the fluorescence was filtered using 430–470, 500–600, and 650–750 nm band-pass filters. For triple-staining imaging, the emission wavelength for imaging was 405, 488, 555, and 647 nm, and the fluorescence was filtered using 430–470, 500–540, 560–620, and 650–750 nm band-pass filters. ".oir" images were obtained with FV3000 and Z-stacked by approximately 1-μm step (1.0–1.4 μm) for microglia and neuron number counts and 0.3-μm step for microglia 3D reconstruction. We counted the number of microglia in the plane image or 5-μm depth stack image within 40–50-μm-depth volume of each brain region and showed the cells per square millimeter (Figs. 1d, e, 2, 5g–l, and 10c, e, f and Supplementary Figs. 1s, 4, and 5b). The numbers of microglia counted in one hundred and forty-four experiments are $n = 5$–41 from 630 planes (: total 10,560 microglia) in CbCrx, $n = 7$–46 from 594 planes (: total 11,859 microglia) in CbN, $n = 11$–41 from 532 planes (: total 11998 microglia) in HPC, $n = 6$–40 from 511 planes (: total 9778 microglia) in VTA, $n = 12$–45 from 590 planes (: total 15767 microglia) in mPFC, and $n = 5$–43 from 550 planes (: total 10455 microglia) in PAG (Figs. 1d, e, 10e, and Supplementary Fig. 4). Several data were not shown due to space limitation and for avoiding redundancy. In HPC we mandatorily took the images of dentate gyrus where the molecular layer (ML), granule cell layer (GCL), and hilus (Hil) exist, and we counted each microglia subtype and obtained the density as the sum. Representative images of microglia in each region (Supplementary Fig. 2) were maximum intensity projections of approximately 10-μm thickness. To quantify Ki67 signal in microglia, we detected Ki67-fluoercent signal in the DAPI-positive nuclei and counted number of Ki67(+) and Iba1(+) cells (Fig. 2b, c). The numbers of microglia counted in forty experiments are $n = 4$–30 Iba1(+) microglia (: total 2943) and $n = 0$–8 Iba1(+)Ki67(+) microglia (: total 299) from 196 planes in CbCrx, $n = 6$–41 Iba1(+) microglia (: total 4224) and $n = 0$–9 Iba1(+) Ki67(+) microglia (: total 551) from 181 planes in CbN, $n = 10$–37 Iba1(+) microglia (: total 4139) and $n = 0$–7 Iba1(+)Ki67(+) microglia (: total 483) from 90 planes in HPC, and $n = 9$–39 Iba1(+) microglia (: total 3699) and $n = 0$–6 Iba1(+)Ki67(+) microglia (: total 481) from 174 planes in VTA (Fig. 2b, c). To quantify Cleaved-Caspase 3 (Clv-Casp3) signaling in microglia, we counted the number of Clv-Casp3 fluorescent signals overlapping with the cell bodies of Iba1-positive cells (Fig. 2e-h). The numbers of microglia counted in forty experiments are $n = 7$–39 Iba1(+) microglia (: total 3005) and $n = 0$–4 Iba1(+)Clv-Casp3(+) microglia (: total 111) from 168 planes in CbCrx, $n = 11$–35 Iba1(+) microglia (: total 3281) and $n = 0$–3 Iba1(+)Clv-Casp3 (+) microglia (: total 111) from 150 planes in CbN, $n = 13$–53 Iba1(+) microglia (: total 3817) and $n = 0$–2 Iba1(+)Clv-Casp3 (+) microglia (: total 106) from 165 planes in HPC, $n = 10$–34 Iba1(+) microglia (: total 3018) and $n = 0$–2 Iba1(+)Clv-Casp3 (+) microglia (: total 73) from 164 planes in VTA (Fig. 2f, g).

For reconstructing 3D microglia (Fig. 3a), we used Imaris 3D/4D microscopy Image Viewer (Oxford Instruments, UK). In the Sholl analysis (Fig. 3b-f, and Supplementary Figs. 7, 8), we analyzed images using Fiji and SNT plugin (Neuroanatomy plugin for Sholl analysis) following the previous protocol[31]. The interaction counts against concentric circles with different radii with 0.5-μm bins were graphed in the Sholl analysis ($n = 14$–30 in CbCrx; $n = 15$–29 in CbN; $n = 16$–27 in mPFC; $n = 14$–30 in VTA; and $n = 14$–30 in HPC). In HPC, we showed only data from the molecular layer but not data from the granule cell layer and hilus in Fig. 3b-f. Data were analyzed using a linear mixed model, which showed a significant difference in the area of CbCrx and CbN in interaction with two-way ANOVA between experimental groups (radius: 10–60 μm) (Fig. 3c-f). In the cerebellum, we used the stacked image of 30–38-μm thickness in total. In VTA, we used 16–20-μm thickness. In the hippocampus, we used 23–27-μm thickness.

For measuring the density of Purkinje cells, Purkinje-cell axons, and microglia from identical sections (Fig. 6), we adopted co-staining with anti-Calbindin and anti-Iba1 antibodies and took volume images from lobules II–IV, VIa–VIb, and IX–X from a sagittal section of cerebellar vermis. We counted the number of Calbindin(+) cells in the Purkinje cell layer of images and divided it with the length of the Purkinje-cell-layer contour (Fig. 6b, male; and Fig. 6g, female). Axon density was obtained from the Calbindin(+) axons in the white matter (Fig. 6c, male; and Fig. 6h, female). Iba1-positive microglia were counted from a stack image of five sections in series (i.e., 5–7 μm thickness) (Fig. 6d, male; and Fig. 6i, female). In Fig. 6e (male) and 6j (female), we applied principal component analysis to three group data and displayed plots.

To confirm the localization of the immune cells detected in imaging mass cytometry, we quantified MHC class II(+) cells and Iba1(+)MHC class II(+)TREM2(+) cells in CbCrx, CbN, HPC, mPFC (Fig. 5g-l) and CbCrx, CbN (Fig. 10f). The numbers of microglia counted in 38 experiments are $n = 3$–38 Iba1(+) microglia (: total 2858) and $n = 0$–4 Iba1(+) MHC class II(+)TREM2(+) microglia (: total 69) from 168 planes in CbCrx, $n = 6$–35 Iba1(+) microglia (: total 3203) and $n = 0$–3 Iba1(+)MHC class II(+)TREM2(+) microglia (: total 27) from 169 planes in CbN, $n = 8$–33 Iba1(+) microglia (: total 2132) and $n = 0$ Iba1(+)MHC class II(+)TREM2(+) microglia from 105 planes in HPC, and $n = 15$–34 Iba1(+) microglia (: total 2829) and $n = 0$ Iba1(+)MHC class II(+)TREM2(+) microglia from 565 planes in mPFC (Figs. 5g-l and 10f).

Cell and axon counting programmings

For counting cells and axons consistently, we developed a program to count the number of microglia and neurons using MATLAB (Supplementary Figs. 3 and 17). To count the cells, we adopted two ways for cell recognition: cell recognition from nuclei position and cell recognition from morphometric properties. For cell recognition from nuclei position, we reduced noise signals from plane or stack images of microglia (i.e., Iba1), neurons (i.e., Calbindin), and nuclei (i.e., DAPI) by FFT/IFFT (fast Fourier transform/inverse fast Fourier transform) preprocessing using Gaussian kernels ($\sigma = 0.5$ μm for microglia or 0.4 μm for nuclei). Next, we extracted the positions of microglia soma and nuclei from denoised images by a Matlab function *imfindcircles*. We detected the microglia position from the superimposed image of nuclei and microglia soma. In cell recognition from morphometric properties, denoised stack images of Iba1 (5 series images) with FFT/IFFT preprocessing (Gaussian kernels: $\sigma = 1$ μm for microglia) were classified by microglia morphology using a Matlab function *regionprops*. We extracted microglia soma position from the denoised image using *imfindcircles*. Combined with morphometric classification, we detected microglia and refined the detection with a fluorescence threshold. For Ki-67(+) microglia detection (Fig. 2a-d), we combined the Iba-1(+) microglia detection with Ki-67 within the signal of nuclei detected by DAPI, respectively. For clv-Casp3(+) microglia detection (Fig. 2e-h), we counted clv-Casp3 signals manually.

For counting neuron and axon numbers in the cerebellar cortex (Supplementary Fig. 17), we applied noise reduction to a plane image of

Calbindin with FFT/IFFT preprocessing using Gaussian kernels ($\sigma = 0.5$ μm for neurons). We extracted neural position from the denoised image and refined cell recognition by omitting the duplication. For axon finding, we set two points for axon detection (i.e., start and end) and obtained fluorescence signals, from which the peaks of signals were detected as the number of axons. Fluorescence signals were normalized with minimum and maximum. We judged local peaks from which the differential function turns from an increase to a decrease, and the polarity of the intermediate value is positive. Local peaks were refined with the threshold of 3.6 times the minimum absolute fluorescence signal and 8% of normalized values. We removed the saturated signals from axon counting.

Imaging mass cytometry

Tissue staining. The conventional immunostaining method with a few numbers of markers does not allow for segregating the cluster of immune cells of efficient classification. The staining procedure for tissue imaging for the Hyperion® imaging system (Standard BioTools™) is similar to standard immunohistochemistry techniques for tissue collection, tissue processing, and staining. 9-week-old male mice were used for the imaging mass cytometry. After perfusion and fixation with 10% formalin, brains were kept in formalin for 2 days at 4 °C. Then, brain tissues were dehydrated, degreased, and embedded in paraffin. Paraffin-embedded tissue blocks were sectioned by 4-μm thickness, attached to a glass slide, and dried at 37 °C for 24 h. We took brain samples from the cerebellar cortex, cerebellar nuclei, VTA, PAG, hippocampus, thalamus, and mPFC of Control, RSDS, MIA, and 2HIT mice ($n = 3$ for each; at 8–10-week-old). After stretching paraffin with a slide-oven, sections were dewaxed in flesh xylene for 20 min (FUJIFILM Wako Pure Chemical Co., Osaka, Japan), and the slides were hydrated in descending grades of ethanol for deparaffinization. After incubation with antigen retrieval solution (Antigen Retrieval Reagent pH 9 (10x), S236784-2 Agilent®) and immersion with 3% BSA (Bovine Serum Albumin, A3059, Sigma-Aldrich) blocking solution, the slides were placed in a hydration chamber and dropped the antibody master mix onto the section encircled with a PAP pen. Instead of using sterile water, we used Maxpar Water and Maxpar PBS (Standard BioTools™) to avoid contamination of a very small amount of metal ingredients. Tissues on the slides were incubated overnight with the antibody cocktail at 4 °C in a hydration chamber. Afterward, slides were washed in 0.2% Triton X-100 in Maxpar PBS and Maxpar PBS. Lastly, for nuclear staining, the tissues were stained with Intercalator-Ir (Cell-ID™ Intercalator-Ir, Standard BioTools™) in Maxpar PBS (80 μL/section of 1:400 solution) for 30 min at room temperature in a hydration chamber.

The antibody cocktail was customized for this study's aim and composed of antibodies: Rabbit anti-alpha smooth muscle actin (αSMA) Polyclonal antibody (abcam, ab5694, RRID: AB_2223021), Rabbit anti-Olig2 Monoclonal antibody (abcam, ab220796, clone: EPR2673, RRID: AB_2923001), Rabbit anti-Iba1 Monoclonal antibody (GeneTex, GTX635363, clone: HL22, RRID: AB_2888516), Rat anti-Sall1 Monoclonal antibody (Invitrogen, 14-9729-82, clone: NRNSTNX, RRID: AB_2848275), Goat anti-MMP-9 Polyclonal antibody (R&D Systems, AF909, RRID: AB_355706), Rabbit anti-MAP2 Polyclonal antibody (abcam, ab32454, RRID: AB_776174), Rat anti-LYVE1 Monoclonal antibody (eBioscience, 14-0443-82, clone: ALY7, RRID: AB_1633414), Rabbit anti-TGFBR2 Polyclonal antibody (Invitrogen, PA5-35076, RRID: AB_2552386), Mouse anti-Claudin 5 Monoclonal antibody (Invitrogen, 35-2500, clone: 4C3C2, RRID: AB_2533200), Mouse anti-GFAP Monoclonal antibody (Invitrogen, 14-9892-82, clone: GA5, RRID: AB_10598206), Rabbit anti-IL6ST/CD130/gp130 Monoclonal antibody (LifeSpan Biosciences, LS-C819329, clone: 223, RRID: AB_2923002), Rabbit anti-IL6 Polyclonal antibody (Biorbyt, orb6210, RRID: AB_10941290), Rabbit anti-Aquaporin 4 Monoclonal antibody (abcam, ab282586, clone: EPR24281-65, RRID: AB_2923003), Rabbit anti-TMEM119 Monoclonal antibody (abcam, ab234501, clone: 28-3, RRID: AB_2923004), Rabbit anti-Caspase-1 Polyclonal antibody (abcam, ab138483, RRID: AB_2888675), Goat anti-PDGF R beta Polyclonal antibody (R&D Systems, AF1042, RRID: AB_2162633), Rabbit anti-Ki67 Polyclonal antibody (abcam, ab15580, RRID: AB_443209), Rabbit anti-TGF-beta 1 Polyclonal antibody (Novus Biologicals, NBP1-80289, RRID: AB_11011860), Rabbit anti-IL-17RA Polyclonal antibody (abcam, ab180904, RRID: AB_2756838), Rabbit anti-TREM2 Polyclonal antibody (Biorbyt, orb7115, RRID: AB_10938677), Rabbit anti-CX3CR1 Polyclonal antibody (Novus Biologicals, NBP1-76949, RRID: AB_11029553), Rat anti-MHC Class II Monoclonal antibody (Novus Biologicals, NB100-64959, clone: ER-TR2, RRID: AB_964544), Mouse anti-Apolipoprotein E Monoclonal antibody (Novus Biologicals, NB110-60531, clone: WUE-4, RRID: AB_920623), and Rabbit anti-IL-17A Polyclonal antibody (abcam, ab79056, RRID: AB_1603584). BSA-, glycerol-, and azide-free antibodies were selected as possible for higher imaging quality and sensitivity.

We selected antibodies listed above to visualize microglia (IBA1, Sall1, TMEM119, CX3CR1, Ki67, TGF-β1, Lyve1, TREM2, MHC-class II, APOE), pericytes (PDGFRβ), astrocytes/BBB (GFAP, AQP4), oligodendrocytes (Olig2), vascular smooth muscle cells (αSMA), endothelial cells (Claudin-5), and neurons (MAP2). To assess the breakdown of vasculature cells, we used MMP-9 to detect basement membrane degeneration. To test apoptosis, we evaluated using an antibody for Caspase-1. We also investigated the expression of cytokines and receptor expression for TGFBR2, IL6ST (gp130), IL-6, IL-17RA, and IL-17. IL6ST (also known as gp-130 or CD130) is the signal transducer of the IL-6 receptor complex. Antibodies for microglia/macrophages were selected based on prior studies[24,26,46,47,52]. Ki67 and TGF-β1 are used to detect immune cell proliferation. However, a limitation in the IMC experiment was the availability of solely BSA-, glycerol-, and azide-free antibodies, which restricted the molecule selection to detect. We conducted pilot staining ($N = 1$, for each condition) or referred to manufacturers' websites for immunohistochemistry (IHC) staining to confirm the concentration to use in IMC, and we determined the adequate concentration of antibodies from three different concentrations and chose the antigen retrieval condition. Note that the recommended concentrations for IHC may differ from those needed for IMC, necessitating quality checks. The discovery of stress-associated microglia/macrophage (SAM) was a serendipitous finding from our steady pilot testing.

Each antibody was manually conjugated to lanthanide (Ln) metals using Maxpar® X8 Antibody Labeling Kit (Standard BioTools™) and following the Maxpar Antibody Labeling User Guide (PRD002 Rev 17, Chapter 3: Maxpar X8 Antibody Labeling Kits). Briefly, the Ln metal solution was loaded to Maxpar X8 polymer, and the antibodies were partially reduced with TCEP (Tris(2-carboxyethyl)phosphine hydrochloride (TCEP) solution, pH 7.0, 646547, Sigma-Aldrich). Both the Ln-loaded polymer and the reduced antibody were conjugated. Ln metal solutions used in our study are followings: Maxpar® X8 Antibody Labeling Kit 141Pr for αSMA, 201141 A; 145Nd for Olig2, 201145 A; 147Sm for IBA1, 201147 A; 149Sm for Sall1, 201149 A; 151Eu for MMP-9, 201151 A; 152Sm for MAP2, 201152 A; 153Eu for Lyve1, 201153 A; 154Sm for TGFBR2, 201154 A; 155Gd for Claudin-5, 201155 A; 158Gd for GFAP, 201158 A; 159Tb for IL6ST, 201159 A; 160Gd for IL-6, 201160 A; 161Dy for AQP4, 201161 A; 164Dy for TMEM119, 201164 A; 165Ho for Caspase-1, 201165 A; 166Er for PDGFR beta, 201166 A; 168Er for Ki67, 201168 A; 169Tm for TGF-β1, 201169 A; 170Er for IL-17RA, 201170 A; 171Yb for TREM2, 201171 A; 172Yb for CX3CR1, 201172 A; 174Yb for MHC-class II, 201174 A; 175Lu for APOE, 201175 A; 176Yb for IL-17, 201176 A. The final concentration of metal-conjugated antibodies are 141Pr-αSMA: 1.25 μg/ml, 145Nd-Olig2: 1.67 μg/ml, 147Sm-IBA1: 25 μg/ml, 149Sm-Sall1: 25 μg/ml, 151Eu-MMP-9: 3.33 μg/ml, 152Sm-MAP2: 1 μg/ml, 153Eu-Lyve1: 10 μg/ml, 154Sm-TGFBR2: 10 μg/ml, 155Gd-Claudin-5: 10 μg/ml, 158Gd-GFAP: 1.67 μg/ml, 159Tb-IL6ST : 0.1 μg/ml, 160Gd-IL-6: 6 μg/ml, 161Dy-AQP4: 2.5 μg/ml, 164Dy-TMEM119: 1.25 μg/ml, 165Ho-Caspase-1: 2.5 μg/ml, 166Er-PDGFR beta: 3.33 μg/ml, 168Er-Ki67: 0.625 μg/ml, 169Tm-TGF-β1: 10 μg/ml, 170Er-IL-17RA: 2 μg/ml, 171Yb-TREM2: 3.33 μg/ml, 172Yb-CX3CR1: 1.67 μg/ml, 174Yb-MHC class II: 10 μg/ml, 175Lu-APOE: 3.33 μg/ml, and 176Yb-IL-17: 2 μg/ml. We determined the final

concentration of metal-conjugated antibodies from the IMC image of one experiment across the brain (cerebellum, hippocampus, and mPFC) by conducting the IMC imaging with three different concentrations of metal-conjugated antibodies and different retrieval conditions, as mentioned above.

In the human postmortem samples of volunteers, brain tissues of the precentral gyrus from a patient with ALS (male, 70-year-old Japanese, died in 2004) and healthy control (male, 54-year-old Japanese, died of pancreatic cancer in 2012), not diagnosed to have suffered from motor or cognitive difficulties in life from his clinical data and treatment history, were formalin-fixed and paraffin-embedded (FFPE) and sectioned by 4-μm thickness as mouse sample. The tissue staining methods are substantially identical to the mouse protocol. For IMC with a human patient's post-mortem brain (Supplementary Fig. 9e), we used the following antibodies for disease-associated microglia/macrophages (DAMs) markers (Mouse anti-Iba1 Monoclonal antibody (Invitrogen, MA5-38265, clone: HL22-MS, RRID: AB_2898181), Rabbit anti-gp130/IL6ST Polyclonal antibody (Sino Biological, 101867-T10, RRID: AB_3094604), Mouse anti-TREM2 Monoclonal antibody (NSJ Bio, V9417SAF, clone: TREM2/7210, RRID: AB_3094605), Mouse anti-Apolipoprotein E (APOE) Monoclonal antibody (abcam, ab1906, clone: D6E10, RRID: AB_302668), and mouse anti-MHC class II Monoclonal antibody (abcam, ab55152, clone: 6C6, AB_944199)). Each antibody was manually conjugated to Ln metals Maxpar® X8 Antibody Labeling Kit 160Gd for Iba1, 201160A; 159Tb for gp130/IL6ST, 201159A; 171Yb for TREM2, 201171 A; 170Er for APOE, 201170A; 174Yb for MHC class II, 201174 A. The final concentrations of metal-conjugated antibodies are 160Gd-Iba1: 6.25 μg/ml, 159T-gp130/IL6ST: 2 μg/ml, 171Yb-TREM2: 6.75 μg/ml, 170Er-APOE: 10 μg/ml, and 174Yb-MHC class II: 13.4 μg/ml.

Imaging acquisition. In both mouse and human samples, the brain-tissue samples and the slides were first taken the image using a smartphone camera to reference the ROIs for the IMC image acquisition. Three to four different ROIs were arbitrarily chosen from each section (cerebellar cortex, cerebellar nuclei, VTA, PAG, hippocampus, thalamus, and mPFC, Fig. 4d-f). Hyperion® imaging system (Standard BioTools™) allows retrieving signals from 24 mass channels for markers of interest in addition to channels for two nuclear markers (Ir191 and Ir193). After adjusting the imaging region of the sample slide using the reference image, images of one to three individual ROIs (maximum size of 1507 μm × 1637 μm, for 3 h) were acquired at the resolution of 1 μm. Acquired IMC images were saved as a separate MathCad (.mcd) file. The MCD Viewer software (v1.0.560.6) visualized mcd-files as images and exported the OME-TIFF 16-bit format.

Mouse 2HIT stress-associated puncta were identified from chosen markers (MHC-class II, IL6ST/gp130, TREM2, TGFBR2, APOE, and MMP-9). All of the markers do not necessarily express in the cells. Therefore, using MHC-class II expression as a starting point, we defined puncta that coexpressed other markers as 2HIT stress-related puncta (Fig. 4d-i). We identified 4284 and 5895 cells from the Control and 2HIT cerebellar cortex, respectively. The cell sizes of the diameter were 11.1 ± 0.2 μm to 13.9 ± 0.6 μm in Control and 12.6 ± 0.2 μm to 14.4 ± 0.2 μm in 2HIT. Human disease-associated puncta were identified from chosen markers (MHC-class II, IL6ST/gp130, TREM2, and APOE) (Supplementary Fig. 9e). The human aged control data is unshown.

Cell segmentation and clustering

Individual tiff images per antibody marker were exported using MCD Viewer. Images for Ir191 and Ir193 were imported into Cell Profiler v4.2.4[81] to obtain the cell mask. Next, we added the nuclei signal of Ir191 and Ir193 with the "ImageMath" module. Then, we used the "IdentifyPrimaryObject" module for the nuclei segmentation, setting the typical diameter of the objects from 5- to 20-pixel units. The segmented nuclei were expanded by the pixel number of three with the Distance-N method to identify the whole-cell objects. We converted the cell objects into images using "ConvertObjectToImage" and saved the image masking the cells. The histoCAT-analysis[82] provides clustering at the single-cell level. The cell mask along with all tiff images was loaded into the histoCAT v1.76 and generated the single-cell data. We excluded the markers from the analysis whose signal intensity wasn't substantially measured in the cells, to avoid the bias of numerical analyses. We also cropped the original IMC image of MIA to exclude a noisy part where the cell segmentation was not done properly. In Supplementary Fig. 11, we provide the signal intensity of the marker molecules of 2HIT SAM, 2HIT immune cell, and Control immune cell in the cerebellum. We validated every classified cell has a prominent signal intensity compared to the void space by plotting cluster-wise mean intensity (Supplementary Fig. 13). We measured the mean IMC signal intensity of each marker signal in both cell-specific and cluster-specific manner. In a cell-specific manner (Supplementary Fig. 11), we selected a representative cell from the control immune cell, 2HIT SAM, and 2HIT immune cell. We measured the intensity with ImageJ using the grayscale image. We created a 100 μm × 100 μm rectangle around the representative cell and measured the mean intensity, followed by the generation of line graphs. In a cluster-specific manner (Supplementary Fig. 13), we first measured the noise signal by extracting intensity values from regions without signal. The noise signal measurement aimed to ensure accurate marker intensity assessment. Then, we calculated the mean intensity of each marker in the cluster and generated a kernel-density plot along with the noise. We further constructed rug plots using Python for the immune cell clusters to get a clear insight into the changes in marker intensity between the immune cell and SAM.

We used the "Phenograph" of the histoCAT for the clustering and generated the heatmap with the mean intensity of each marker for annotating clusters. We identified 4284, 4980, 5693, and 5895 cells from Control, RSDS, MIA, and 2HIT cerebellar cortex, respectively (Fig. 5a as 2HIT, and Supplementary Fig. 12a as Control, 12e as RSDS, 12i as MIA). The area and cell sizes of the diameter were given as the result, the numbers of cells in individual clusters were $N = 20–692$ of 12 clusters in Control, $N = 33–991$ of 11 clusters in RSDS, $N = 120 – 1038$ of 11 clusters in MIA, and $N = 51–844$ of 14 clusters in 2HIT, respectively. Lastly, we employed tSNE for cluster visualization. We annotated clusters from the marker molecules and spatial distribution of the brain region (e.g., from the layer and location of the tissue). In the 2HIT single-cell dataset, disorder-associated immune cell clusters, including SAM, were characterized.

We performed the Potential of Heat-diffusion Affinity-based Transition Embedding (PHATE)[83] mapping to study the cell state transition of the multi-dimensional marker expression pattern (Supplementary Fig. 14b-e). We used the Markov affinity-based graph imputation of cells (MAGIC)[84] method for denoising and restoring the structure of the data before using PHATE. We pre-processed data with MinMaxScaler of Sklearn implemented in Python for normalization. The MAGIC algorithm was executed with the parameters as their default specifications. Then, the output data was imported into the PHATE algorithm implemented in Python for the cell transition analysis. The optimized diffusion operator "t" and decay value were selected after several iterations. The other parameters were left as default. All the cells except the immune cells were excluded from the analysis. Plots were generated with the Python Seaborn package (Supplementary Fig. 14b-e). To evaluate the stability and cell transition possibility among clusters in the PHATE space, we defined the transition entropy: $= -\Sigma_{pairs}(d*\log(d))/$ number of pairs, where d:= distance of each pair of cells in the PHATE space as Euclidean distance. In Supplementary Fig. 14b-e, we depicted circles of PHATE transition entropy at the gravity center of the clusters. The radii of circles indicate the entropy size. The entropy is the measure of uncertainty and disorder. When the PHATE entropy is large, the measure of the total amount of disorder in the protein expression pattern is large, meaning variable and unstable state. Kullback–Leibler divergence is the difference between entropy.

For cell-cell pairwise distance analysis (Supplementary Figs. 15 and 16), we measured the Euclidian distance of each cell pair between the clusters, excluding the clusters of neurons. After single cell classification, we extracted cell populations of clusters except for neurons (Supplementary Figs. 15a,d

and 16a,c). The annotation of each cluster is identical to Fig. 5c (2HIT) and Supplementary Figs. 12c (Control). Then, we generated the histogram using the cell-cell pairwise distance matrix between clusters. We considered two clusters localized closely if there is any peak within 100 μm (red or black vertical lines in Supplementary Figs. 15b,e and 16b,d). Some clusters in Control and 2HIT have a peak within 100 μm, however, no peak was found at the threshold for MIA and RSDS. The red rectangles around the histogram indicate there is a peak within 100 μm between clusters. To test whether the peak occurs by chance, we performed a bootstrap test followed by a two-sampled Kolmogorov-Smirnov (KS) test. We created a randomized dataset by combining two clusters and shuffling the cells. Then, we divided the randomized dataset into two populations with the same length as the original clusters and generated the distance matrix between them. We tested the significant difference between this randomized distance matrix and the original distance matrix with the two-sampled KS test at the significant level of 0.01. Any significant difference indicates the peak does not occur by chance. We repeated this step 2000 times and requested for the false negative rate. When the error is less than 0.05 for 2000 iterations, we considered them significantly different.

We performed a mixture analysis to compare the cell population between the control and 2HIT models through batch correction and integration of the dataset (Fig. 5e,f). We annotated both datasets adding the batch information and then combined them to create a single integrated dataset. We performed batch effect correction by employing pyComBat to mitigate any batch-related variations in the integrated dataset. We used Phenograph for the clustering of the corrected dataset to identify distinct cell populations. We employed tSNE for the dimension reduction and visualization and generated the heatmap with the corrected mean intensity of each marker for the annotation of the cluster. We further created a volcano plot to get the changes in the protein expression between the immune cells and the SAM cluster. We calculated the log2 fold change of the SAM cluster with the immune cell cluster and measured the *p*-value for each marker with two-sample Student's *t*-test between the immune cell and SAM cluster.

Patch-clamp recordings

Purkinje cells. In vitro, patch-clamp recordings from cerebellar Purkinje cells were done according to the previous study[44]. Sagittal slices of the cerebellar vermis (250 μm) were prepared from male Control, RSDS susceptible, MIA, 2HIT susceptible, and 2HIT+rMG and female Control, 2HIT susceptible, 2HIT resilient, and 2HIT+rMG C57BL/6N mice (9–12 weeks old) after isoflurane anesthesia and decapitation (Fig. 7). Slices were cut on a vibratome (Dosaka EM, Japan) using ceramic blades. Subsequently, slices were kept in artificial cerebrospinal fluid (ACSF) containing the following (in mM): 124 NaCl, 5 KCl, 1.25 Na_2HPO_4, 2 $MgSO_4$, 2 $CaCl_2$, 26 $NaHCO_3$, and 10 $_D$-glucose, bubbled with 95% O_2 and 5% CO_2. During cutting, supplemental ingredients (5 mM Na-ascorbate, 2 mM thiourea, and 3 mM Na-pyruvate) were added to the ACSF. After at least 1-h recovery, slices were transferred to a recording chamber submerged with ACSF at near-physiological temperature (32–34 °C). The ACSF was supplemented with 100 μM picrotoxin to block the chloride channel gated by $GABA_A$ receptors and 20 μM NBQX disodium salt to block AMPA receptors. Patch-clamp recordings were performed under a ×40-water immersion objective lens equipped with a DIC system (DS-Qi2; Nikon) mounted on a microscope (ECLIPSE FN1, Nikon). Recordings were performed in voltage-clamp or current-clamp mode using an EPC-10 amplifier (HEKA Elektronik GmbH, Germany). Membrane voltage and current were filtered at 2.9 kHz, digitized at 10 kHz, and acquired using Patchmaster software (HEKA Elektronik). Patch pipettes (borosilicate glass) were filled with a solution containing (in mM): 9 KCl, 10 KOH, 120 K-gluconate, 3.48 $MgCl_2$, 10 HEPES, 4 NaCl, 4 Na_2ATP, 0.4 Na_3GTP, and 17.5 sucrose (pH 7.25 titrated with 1 M KOH). Membrane voltage was offset for liquid junction potentials (11.7 mV). Somatic patch electrodes had electrode resistances of 4–5 MΩ[44,85]. Hyperpolarizing bias currents (100–400 pA) were injected to stabilize the membrane potential at ~−72 to −80 mV and to prevent spontaneous spike activity. We applied the bridge balance under the current clamp. A balanced bridge for the correction of membrane voltage errors is to inject current from the amplifier through the resistance of the pipette for measuring the true membrane voltage. To turn the bridge on using the HEKA EPC-10 amplifier and PATCHMASTER, we set the time constant to 10 μs and set the percentage control to 100%. Then, the bridge compensates exactly the value of the R-series. To obtain the firing frequency in response to different levels of depolarization (Fig. 7a, b, p, q), we applied 500-ms pulses ranging from 0 to 550 pA every 2 or 3 s, which were increased by 50 pA per step, and counted the number of simple spike-shaped action potentials. We repeated experiments and took data in 20–30 cells from 5 to 7 animals of each conditioning.

Layer 5 pyramidal cells

In vitro patch-clamp recordings from cerebral L5 were obtained according to the previous study[76] (Supplementary Fig. 20). Coronal sections of the cerebral prefrontal cortex (250 μm) at the position of +0.5- to +2.0-mm caudal from the bregma were prepared from male control and 2HIT C57BL/6 N mice. The slices were kept in ACSF containing the following (in mM): 124 NaCl, 5 KCl, 1.25 Na_2HPO_4, 2 $MgSO_4$, 2 $CaCl_2$, 26 $NaHCO_3$, and 25 $_D$-glucose, bubbled with 95% O_2 and 5% CO_2. Borosilicate glass pipettes were filled with K-gluconate solution which contains (in mM): 9 KCl, 10 KOH, 120 K-gluconate, 10 HEPES, 4 MgATP, 0.4 Na_3GTP, 10 Na_2-phosphocreatine, and 17.5 sucrose (pH 7.25 titrated with 1 M KOH). Membrane voltage was offset for liquid junction potential (11.7 mV for K-gluconate solution). The somatic patch electrodes had electrode resistances of 4 – 6 MΩ. After sealing and breaking the cell membrane under the voltage-clamp mode at −71.7 mV, bias currents (−100 to +50 pA) were injected to stabilize the somatic membrane potential. Then, we switched the recording to current-clamp mode, and the membrane potential was held at ~−72 mV. We applied the bridge balance under the current clamp. We repeated experiments and took data in 20–30 cells from 4 animals of each conditioning.

Electrophysiological data analysis

Data were analyzed using a custom program written in MATLAB (Mathworks, USA). For the analysis of action-potential waveforms, we measured the first action potential evoked by the administration of 200–400-pA depolarizing pulses, manually. Action potential analysis was performed according to the previous study[44] (Fig. 7c-o, r-ac and Supplementary Fig. 20c-p).

fMRI

Mouse MR imaging and data analyses. 10–11-week-old male Control ($n = 15$), RSDS ($n = 15$), MIA ($n = 14$), and 2HIT ($n = 15$) mice inhaled isoflurane (2% for induction: 1% for MR imaging (MRI)) in a mixture of 66% air and 34% oxygen at 1.5 L/min with ventilation, were stabilized by head-holding in a plastic tube and were monitored for respiratory rate (105–142 breaths/min) and body temperature (32–34 °C). Mice were scanned with a 7.0 T MRI scanner (Bruker BioSpin) with a quadrature transmit-receive volume coil (35 mm inner diameter). To make the main magnetic field more homogeneous, shimming was performed in a $12 \times 8 \times 5$ mm^3 region employing a local MapShim protocol using a previously acquired field map. Resting-state *f*MRI is a method to study the functional network in the brain from spontaneous activity without any external stimulation. Spontaneous low-frequency fluctuations (<0.1 Hz) in the blood-oxygen-level dependent (BOLD) signals of some regions are known to synchronize with each other. Such correlation of the BOLD signals is considered a manifestation of functional connectivity of the brain. BOLD rs-*f*MRI time series were obtained with a single-shot gradient-echo planar imaging (EPI) sequence (repetition time [TR]/echo time [TE] = 1.0 s/9 ms; flip angle, 60°; matrix size, 80×64; field of view [FOV], 1.80×1.44 cm^2; 12 coronal slices from top to bottom; slice thickness, 0.75 mm; slice gap 0 mm) for 8 min with a total 480 volumes. Following the EPI sequence three times, high-resolution anatomical

images for each experimental animal were obtained using a 2D multi-slice T_2-weighted (T2W) fast-spin echo sequence (RARE) (TR/TE = 3.0 s/36 ms; matrix size, 180 × 144; FOV, 1.80 × 1.44 cm; 18 coronal slices; slice thickness, 0.50 mm; slice gap 0 mm; with fat suppression by frequency selective pre-saturation) under 2.0% isoflurane inhalation. In the cerebellum of anesthetized living rodents, the increased pace-making spike activity of Purkinje cells and spontaneous local field potentials per se is not sufficient to affect basal cerebral blood flow (CBF) and, in turn, BOLD signals[71,86]. Rather, CBF is known to couple with field potentials evoked by afferent fiber activation[71].

Image data were analyzed with SPM12 (https://www.fil.ion.ucl.ac.uk/spm/) and in-house software written with MATLAB (MathWorks). We pre-processed imaging data according to the previous study[44]. First, the EPIs were realigned and co-registered to a template brain using anatomical images. A T2W anatomical image was used as a template brain. Co-registered functional EPIs were normalized to the template and transformed to a 151 × 91 × 81 matrix (with a spatial resolution of 0.20 × 0.20 × 0.20 mm^3) and smoothed with a Gaussian kernel (full width at half maximum [FWHM], 0.7 mm). We manually omitted data with motion artifacts (26 scans in total). Imaging data were temporally zero-phase band-pass filtered to retain low-frequency components (0.01–0.10 Hz) using the *filtfilt* Matlab function. For a given time series, seed ROIs (0.4 × 0.4 × 0.2 mm^3) in the 90 seed positions were selected, and the signals in the seed were averaged. Respective seed coordinates are shown in Supplementary Data 1. For ClbHs, ClbFasNc, ClbDnNc, MVN, Pon, Ponc, PAG, SC, RetN, SubN, VTN, HpVL, HpDC, ThlCMDM, ThlVnt, ThlAnt, HypThLZ, HypTh, AmyCe, Pallid, Cadput, NucAcm, Pirif, aI, Ob, mPF, Cg, M1, S1, A1, V1, Ent, ThlVM, BST, LSX, PT, LH, GVIS, and Oa, seeds were applied in both right and left hemispheres. Individual correlation maps (r map at the zeroth lag) were computed by cross-correlation against the mean seed signal to signals of all the other voxels. Then, correlation maps were transformed to normally distributed z scores by Fisher's r-to-z transformation. Z-transformation was used to reflect the strength of spontaneous correlations more linearly at high r values. The resulting group maps were thresholded at $|r| > 0.1$, followed by a cluster-level multiple comparison correction at a significance level of $p < 0.001$ of a one-sample t-test with Kα > 29 voxels. Seed–seed correlation matrices were calculated from all pairs among brain regions for each subject. The correlation matrix was z-transformed. One-sample *t-test* matrix across experiments was thresholded at $p < 0.05$ and was corrected by the Benjamini-Hochberg (BH) procedure to avoid the incorrect rejection of a true null hypothesis (a type I error) with a false discovery rate at $q = 0.05$. Mean seed-seed correlation of the z-matrix was filtered by the T-matrix from the BH procedure and variance-corrected color maps were shown (Fig. 8a-c).

Transmission electron microscope

Animals (10–11-week-old male mice) were anesthetized with an intraperitoneal injection of an anesthetizer mixture containing 0.9% ketamine (Daiichi Sankyo Co., Ltd.) and 0.2% xylazine (Bayer AG), and were perfused transcardially with 0.1 M PB followed by a fixative containing 2% PFA and 2.5% glutaraldehyde in 0.1 M PB. Brains were harvested, cut at 0.5-mm-thick with a slicer Neo-LinearSlicer AT (Dosaka EM, Kyoto, Japan), and fixed with the same fixative for 2 h at 4 °C. Slices were post-fixed with 1% OsO_4 in 0.1 M PB, dehydrated with alcohol, and embedded in epoxy resin. Ultra-thin sections (80-nm-thick) were cut and electron stained with 1% uranyl acetate and Sato's lead staining solution. Specimens were observed with a transmission electron microscope JEM-1400A (JEOL, Tokyo, Japan). G-ratio was calculated as the ratio of the inner axon radius to the outer myelinated axon radius (Fig. 8d-f and Supplementary Fig. 21).

Statistics and reproducibility

Statistical analysis, including mean values, SEM values, and p values, was calculated using MATLAB (MathWorks). Statistical significance between the two groups was evaluated by two-tailed unpaired Student's *t*-test, Wilcoxon rank sum test, or Kolmogorov-Smirnov test. For more than two groups, one-way and two-way ANOVA with Tukey-Kramer or Bonferroni method post-test or MANOVA was performed. In the two-way ANOVA, when the interaction effect was not significant ($p > 0.001$), we compared the main effects. P values below the significance levels specified for each experiment, based on the statistical method used (0.05: Figs. 1d, 1e, 2b-d, 2f-h, 5h, 5i, 5k, 5l, 6b-d, 6g-i, 7d-o, 7r-ac, 9a-j, 9l-t, 9v, 9w, 10c, 10e-g, 10j-w, 10y, 10z, Supplementary Figs. 1b-e, 1j, 1o-q, 1s, 4, 5b, 18, 19, 20d-p, 22, and 23. 0.01: Supplementary Fig. 21. 0.001: Fig. 8d. 0.0001: Figs. 3c-f, 6e, 6j, 7b, 7q, 9k, 9u, 10i, 10x, Supplementary Figs. 7, 8, and 20b. 0.05 + 0.01 + 0.001: Fig. 9x-z (*, **, and ***, respectively). 0.05 + 0.001: Supplementary Fig. 1f and 1k (* and **, respectively).) were considered statistically significant (*). All data are presented as mean ± SEM unless otherwise stated. N represents the number of biological replicates unless otherwise stated. Exact sample size and replication are presented in Supplementary Data.

Data availability

Source Data that support the findings of this study are attached as Supplementary Data and available from the Lead Contact upon request.

Code availability

Custom Matlab codes for analyses in this study are available from the Lead Contact upon individual request.

Received: 25 June 2024; Accepted: 15 January 2025;
Published online: 03 March 2025

References

1. Giovanoli, S. et al. Stress in puberty unmasks latent neuropathological consequences of prenatal immune activation in mice. *Science* **339**, 1095–1099 (2013).
2. Debost, J. P. et al. Joint effects of exposure to prenatal infection and peripubertal psychological trauma in schizophrenia. *Schizophr. Bull.* **43**, 171–179 (2017).
3. Laskaris, L. E. et al. Microglial activation and progressive brain changes in schizophrenia. *Br. J. Pharmacol.* **173**, 666–680 (2016).
4. Khandaker, G. M. et al. Inflammation and immunity in schizophrenia: implications for pathophysiology and treatment. *Lancet Psychiatry* **2**, 258–270 (2015).
5. Yolken, R. H. & Torrey, E. F. Viruses, schizophrenia, and bipolar disorder. *Clin. Microbiol. Rev.* **8**, 131–145 (1995).
6. Colonna, M. & Butovsky, O. Microglia function in the central nervous system during health and neurodegeneration. *Annu. Rev. Immunol.* **35**, 441–468 (2017).
7. Pape, K. et al. Immunoneuropsychiatry—novel perspectives on brain disorders. *Nat. Rev. Neurol.* **15**, 317–328 (2019).
8. Ozaki, A. et al. Psychosis symptoms following aberrant immunity in the brain. *Neural. Regen. Res.* **16**, 512–513 (2021).
9. Smith, S. E. et al. Maternal immune activation alters fetal brain development through interleukin-6. *J. Neurosci.* **27**, 10695–10702 (2007).
10. Parker-Athill, E. C. & Tan, J. Maternal immune activation and autism spectrum disorder: interleukin-6 signaling as a key mechanistic pathway. *Neurosignals* **18**, 113–128 (2010).
11. Mueller, F. S. et al. Influence of poly(I:C) variability on thermoregulation, immune responses and pregnancy outcomes in mouse models of maternal immune activation. *Brain Behav. Immun.* **80**, 406–418 (2019).
12. Purves-Tyson, T. D. et al. Increased levels of midbrain immune-related transcripts in schizophrenia and in murine offspring after maternal immune activation. *Mol. Psychiatry* **26**, 849–863 (2021).
13. Krishnan, V. et al. Molecular adaptations underlying susceptibility and resistance to social defeat in brain reward regions. *Cell* **131**, 391–404 (2007).
14. Feder, A. et al. Psychobiology and molecular genetics of resilience. *Nat. Rev. Neurosci.* **10**, 446–457 (2009).

15. Bayer, T. A. et al. Genetic and non-genetic vulnerability factors in schizophrenia: the basis of the "two hit hypothesis. *J. Psychiatr. Res.* **33**, 543–548 (1999).
16. Maynard, T. M. et al. Neural development, cell-cell signaling, and the "two-hit" hypothesis of schizophrenia. *Schizophr. Bull.* **27**, 457–476 (2001).
17. Comer, A. L. et al. The Inflamed Brain in Schizophrenia: The Convergence of Genetic and Environmental Risk Factors That Lead to Uncontrolled Neuroinflammation. *Front. Cell. Neurosci.* **14**, 274 (2020).
18. Šišková, Z. & Tremblay, M. È. Microglia and synapse: interactions in health and neurodegeneration. *Neural. Plast.* **2013**, 425845 (2013).
19. Hickman, S. et al. Microglia in neurodegeneration. *Nat. Neurosci.* **21**, 1359–1369 (2018).
20. Kettenmann, H. et al. Physiology of microglia. *Physiol. Rev.* **91**, 461–553 (2011).
21. Thion, M. S. et al. Microglia and early brain development: an intimate journey. *Science* **362**, 185–189 (2018).
22. Prinz, M. et al. Microglia biology: one century of evolving concepts. *Cell* **179**, 292–311 (2019).
23. Cathomas, F. et al. Beyond the neuron: role of non-neuronal cells in stress disorders. *Neuron* **110**, 1116–1138 (2022).
24. Deczkowska, A. et al. Disease-associated microglia: a universal immune sensor of neurodegeneration. *Cell* **173**, 1073–1081 (2018).
25. Paolicelli, R. C. et al. Microglia states and nomenclature: a field at its crossroads. *Neuron* **110**, 3458–3483 (2022).
26. Keren-Shaul, H. et al. A unique microglia type associated with restricting development of Alzheimer's disease. *Cell* **169**, 1276–1290.e17 (2017).
27. Masuda, T. et al. Spatial and temporal heterogeneity of mouse and human microglia at single-cell resolution. *Nature* **566**, 388–392 (2019).
28. Utz, S. G. et al. Early fate defines microglia and non-parenchymal brain macrophage development. *Cell* **181**, 557–573.e18 (2020).
29. VanRyzin, J. W. et al. Microglial phagocytosis of newborn cells is induced by endocannabinoids and sculpts sex differences in juvenile rat social play. *Neuron* **102**, 435–449.e6 (2019).
30. Kreisel, T. et al. Dynamic microglial alterations underlie stress-induced depressive-like behavior and suppressed neurogenesis. *Mol. Psychiatry* **19**, 699–709 (2014).
31. Hayes, L. N. et al. Prenatal immune stress blunts microglia reactivity, impairing neurocircuitry. *Nature* **610**, 327–334 (2022).
32. Gober, R. et al. Microglia activation in postmortem brains with schizophrenia demonstrates distinct morphological changes between brain regions. *Brain Pathol.* **32**, e13003 (2022).
33. Schmahmann, J. D. & Sherman, J. C. The cerebellar cognitive affective syndrome. *Brain* **121**, 561–579 (1998).
34. Dean, S. L. & McCarthy, M. M. Steroids, sex and the cerebellar cortex: implications for human disease. *Cerebellum* **7**, 38–47 (2008).
35. Andreasen, N. C. & Pierson, R. The role of the cerebellum in schizophrenia. *Biol. Psychiatry* **64**, 81–88 (2008).
36. Tsai, P. T. et al. Autistic-like behaviour and cerebellar dysfunction in Purkinje cell Tsc1 mutant mice. *Nature* **488**, 647–651 (2012).
37. Piochon, C. et al. Cerebellar plasticity and motor learning deficits in a copy-number variation mouse model of autism. *Nat. Commun.* **5**, 5586 (2014).
38. Hansel, C. et al. Beyond parallel fiber LTD: the diversity of synaptic and non-synaptic plasticity in the cerebellum. *Nat. Neurosci.* **4**, 467–475 (2001).
39. Kano, M. & Hashimoto, K. Synapse elimination in the central nervous system. *Curr. Opin. Neurobiol.* **19**, 154–161 (2009).
40. Ohtsuki, G. et al. Synergistic excitability plasticity in cerebellar functioning. *FEBS J.* **287**, 4557–4593 (2020).
41. Marín-Teva, J. L. et al. Microglia promote the death of developing Purkinje cells. *Neuron* **41**, 535–547 (2004).
42. Stowell, R. D. et al. Cerebellar microglia are dynamically unique and survey Purkinje neurons in vivo. *Dev. Neurobiol.* **78**, 627–644 (2018).
43. Nakayama, H. et al. Microglia permit climbing fiber elimination by promoting GABAergic inhibition in the developing cerebellum. *Nat. Commun.* **9**, 2830 (2018).
44. Yamamoto, M. et al. Microglia-triggered plasticity of intrinsic excitability modulates psychomotor behaviors in acute cerebellar inflammation. *Cell Rep.* **28**, 2923–2938.e8 (2019).
45. Elmore, M. R. et al. Colony-stimulating factor 1 receptor signaling is necessary for microglia viability, unmasking a microglia progenitor cell in the adult brain. *Neuron* **82**, 380–397 (2014).
46. Van Hove, H. et al. A single-cell atlas of mouse brain macrophages reveals unique transcriptional identities shaped by ontogeny and tissue environment. *Nat. Neurosci.* **22**, 1021–1035 (2019).
47. Silvin, A. et al. Dual ontogeny of disease-associated microglia and disease inflammatory macrophages in aging and neurodegeneration. *Immunity* **55**, 1448–1465.e6 (2022).
48. Zeng, H. et al. Integrative in situ mapping of single-cell transcriptional states and tissue histopathology in a mouse model of Alzheimer's disease. *Nat. Neurosci.* **26**, 430–446 (2023).
49. Chiu, I. M. et al. A neurodegeneration-specific gene-expression signature of acutely isolated microglia from an amyotrophic lateral sclerosis mouse model. *Cell Rep.* **4**, 385–401 (2013).
50. Leyns, C. E. G. et al. TREM2 deficiency attenuates neuroinflammation and protects against neurodegeneration in a mouse model of tauopathy. *Proc. Natl. Acad. Sci. USA* **114**, 11524–11529 (2017).
51. Spiller, K. J. et al. Microglia-mediated recovery from ALS-relevant motor neuron degeneration in a mouse model of TDP-43 proteinopathy. *Nat. Neurosci.* **21**, 329–340 (2018).
52. Mrdjen, D. et al. High-dimensional single-cell mapping of central nervous system immune cells reveals distinct myeloid subsets in health, aging, and disease. *Immunity* **48**, 380–395.e6 (2018).
53. Shi, L. et al. Activation of the maternal immune system alters cerebellar development in the offspring. *Brain Behav. Immun.* **23**, 116–123 (2009).
54. Vacher, C. M. et al. Placental endocrine function shapes cerebellar development and social behavior. *Nat. Neurosci.* **24**, 1392–1401 (2021).
55. Ayata, P. et al. Epigenetic regulation of brain region-specific microglia clearance activity. *Nat. Neurosci.* **21**, 1049–1060 (2018).
56. Weber-Stadlbauer, U. et al. Transgenerational modification of dopaminergic dysfunctions induced by maternal immune activation. *Neuropsychopharmacology* **46**, 404–412 (2021).
57. Kawatake-Kuno, A. et al. Sustained antidepressant effects of ketamine metabolite involve GABAergic inhibition-mediated molecular dynamics in aPVT glutamatergic neurons. *Neuron* **112**, 1265–1285.e10 (2024).
58. Kana, V. et al. CSF-1 controls cerebellar microglia and is required for motor function and social interaction. *J. Exp. Med.* **216**, 2265–2281 (2019).
59. Willis, E. F. et al. Repopulating microglia promote brain repair in an IL-6-dependent manner. *Cell* **180**, 833–846.e16 (2020).
60. Yeh, F. L. et al. TREM2 binds to apolipoproteins, including APOE and CLU/APOJ, and thereby facilitates uptake of amyloid-beta by microglia. *Neuron* **91**, 328–340 (2016).
61. Jaitin, D. A. et al. Lipid-associated macrophages control metabolic homeostasis in a Trem2-dependent manner. *Cell* **178**, 686–698.e14 (2019).
62. Krasemann, S. et al. The TREM2-APOE pathway drives the transcriptional phenotype of dysfunctional microglia in neurodegenerative diseases. *Immunity* **47**, 566–581.e9 (2017).
63. Jonsson, T. et al. Variant of TREM2 associated with the risk of Alzheimer's disease. *N. Engl. J. Med.* **368**, 107–116 (2013).
64. van Lengerich, B. et al. A TREM2-activating antibody with a blood-brain barrier transport vehicle enhances microglial metabolism in Alzheimer's disease models. *Nat. Neurosci.* **26**, 416–429 (2023).
65. Whitney, E. R. et al. Cerebellar Purkinje cells are reduced in a subpopulation of autistic brains: a stereological experiment using calbindin-D28k. *Cerebellum* **7**, 406–416 (2008).

66. Crucitti, J. et al. Are vermal lobules VI–VII smaller in autism spectrum disorder? *Cerebellum* **19**, 617–628 (2020).
67. Laidi, C. et al. Cerebellar volume in schizophrenia and bipolar I disorder with and without psychotic features. *Acta Psychiatr. Scand.* **131**, 223–233 (2015).
68. Moberget, T. et al. Cerebellar volume and cerebellocerebral structural covariance in schizophrenia: a multisite mega-analysis of 983 patients and 1349 healthy controls. *Mol. Psychiatry* **23**, 1512–1520 (2018).
69. Baek, S. J. et al. VTA-projecting cerebellar neurons mediate stress-dependent depression-like behaviors. *Elife* **11**, e72981 (2022).
70. Vaaga, C. E. et al. Cerebellar modulation of synaptic input to freezing-related neurons in the periaqueductal gray. *Elife* **9**, e54302 (2020).
71. Thomsen, K. et al. Principal neuron spiking: neither necessary nor sufficient for cerebral blood flow in rat cerebellum. *J. Physiol.* **560**, 181–189 (2004).
72. Schalbetter, S. M. et al. Adolescence is a sensitive period for prefrontal microglia to act on cognitive development. *Sci. Adv.* **8**, eabi6672 (2022).
73. Verpeut, J. L. et al. Cerebellar contributions to a brainwide network for flexible behavior in mice. *Commun. Biol.* **6**, 605 (2023).
74. Snijders, G. J. L. J. et al. A loss of mature microglial markers without immune activation in schizophrenia. *Glia* **69**, 1251–1267 (2021).
75. Coughlin, J. M. et al. Neuroinflammation and brain atrophy in former NFL players: An in vivo multimodal imaging pilot study. *Neurobiol. Dis.* **74**, 58–65 (2015).
76. Yamawaki, Y. et al. Microglia-triggered hypoexcitability plasticity of pyramidal neurons in the rat medial prefrontal cortex. *Curr. Res. Neurobiol.* **3**, 100028 (2022).
77. Fukudome, D. et al. Translocator protein (TSPO) and stress cascades in mouse models of psychosis with inflammatory disturbances. *Schizophr. Res.* **197**, 492–497 (2018).
78. Nie, X. et al. The innate immune receptors TLR2/4 mediate repeated social defeat stress-induced social avoidance through prefrontal microglial activation. *Neuron* **99**, 464–479 (2018).
79. Harris, A. Z. et al. A Novel Method For Chronic Social Defeat Stress In Female Mice. *Neuropsychopharmacology* **43**, 1276–1283 (2018).
80. Ohno, H. et al. A c-fms tyrosine kinase inhibitor, Ki20227, suppresses osteoclast differentiation and osteolytic bone destruction in a bone metastasis model. *Mol. Cancer Ther.* **5**, 2634–2643 (2006).
81. Stirling, D. R. et al. CellProfiler 4: improvements in speed, utility and usability. *BMC bioinform.* **22**, 1–11 (2021).
82. Schapiro, D. et al. histoCAT: analysis of cell phenotypes and interactions in multiplex image cytometry data. *Nat. Methods* **14**, 873–876 (2017).
83. Moon, K. R. et al. Visualizing structure and transitions in high-dimensional biological data. *Nat. Biotechnol.* **37**, 1482–1492 (2019).
84. van Dijk, D. et al. Recovering gene interactions from single-cell data using data diffusion. *Cell* **174**, 716–729.e27 (2018).
85. Ohtsuki, G. et al. SK2 channel modulation contributes to compartment-specific dendritic plasticity in cerebellar Purkinje cells. *Neuron* **75**, 108–120 (2012).
86. Thomsen, K. et al. Principal cell spiking, postsynaptic excitation, and oxygen consumption in the rat cerebellar cortex. *J. Neurophysiol.* **102**, 1503–1512 (2009).

Acknowledgements

We deeply appreciate Prof. Akira Sawa (Johns Hopkins University School of Medicine, USA), Dr. Lindsay Hayes (Johns Hopkins University School of Medicine), Dr. Shusaku Uchida (Nagoya City University Graduate School of Medical Sciences, Japan), and Prof. Christian Hansel (Univ. of Chicago, USA) for their invaluable comments and support of the research. We thank M. Taguchi, R. Toyoda, H. Kanamori, K. Segawa, K. Tanigaki, S. Matsui, K. Nimura, M. Irie, M. Yang, and T. Kawano, for their assistance in experiments and analyses. We also appreciate Sumitomo Pharma Co., Ltd., ONO PHARMACEUTICAL CO., LTD., Mitsubishi Tanabe Pharma Corporation., and KYORIN Pharmaceutical Co., Ltd., as the sponsors for the Department of Drug Discovery Medicine. We thank Dr. Kyoko Yoshikawa (Takeda Pharmaceutical Company Limited) for the collaborative work and suggestions. This work was supported by grants from the Mitsubishi Foundation (G.O.), the Takeda Science Foundation (G.O.), Takeda Pharmaceutical Company Limited (G.O.), JSPS Kakenhi Grant-in-Aid for Scientific Research (B) (19H03547) (T.S. and G.O.), Grant-in-Aid for Scientific Research (C) (23K05978) (G.O.), Japan Agency for Medical Research and Development (AMED) (JP24gm6910013 & JP24zf0127010 (G.O.) and JP23wm0425019 (M.Y. & Japan Brain Bank Net), and JSPS WISE program "The Graduate Program for Medical Innovation (MIP)" (Y.Y. and M.H., respectively).

Author contributions

The funders had no role in the study design, data collection, data analysis, decision to publish, or preparation of the manuscript. G.O., T.S., and S.N. designed the experiments. Experiments were done by the following contributors [Animal production and behavior: Y.Y., and M.H. Immunostaining and analysis: M.H., S.O., Y.L., Y.Y., Md S.A.P., and G.O. Imaging mass cytometry: G.O., Y.W., M.H., and A.K. IMC data analyses: Md S.A.P., and G.O. Electrophysiology: G.O., and M.H. Electron microscopy: T.K., Y.H., and G.O. fMRI: H.I., and G.O. Network models: O.I. Brain-region-specific microglia depletion: M.H., and S.S. Human brain sample preparation: M.Y.]. G.O., M.H., Md S.A.P., M.K., S.O., Y.Y., Y.H., T.K., T.S., S.S., U.M., and S.N. wrote the original manuscript for submission. M.H., and G.O. revised the manuscript and conducted all revision experiments.

Competing interests

The authors declare no competing interests.

Additional information

Supplementary information The online version contains supplementary material available at https://doi.org/10.1038/s42003-025-07566-2.

Correspondence and requests for materials should be addressed to Gen Ohtsuki.

Peer review information *Communications Biology* thanks Marie-Eve Tremblay and the other, anonymous, reviewers for their contribution to the peer review of this work. Primary Handling Editor: Benjamin Bessieres. A peer review file is available.